

# TECHNICAL NOTE

## D-1170

INVESTIGATION OF THE PERFORMANCE OF A  $78^{\circ}$

FLAT-PLATE HELICAL INDUCER

By Richard F. Soltis, Douglas A. Anderson,  
and Donald M. Sandercock

Lewis Research Center  
Cleveland, Ohio

NATIONAL AERONAUTICS AND SPACE ADMINISTRATION  
WASHINGTON

March 1962



# CONTENTS

	Page
SUMMARY . . . . .	1
INTRODUCTION . . . . .	1
APPARATUS AND PROCEDURE . . . . .	3
Test Rotor . . . . .	3
Test Facility . . . . .	3
Instrumentation . . . . .	3
Procedure . . . . .	4
Calculations . . . . .	5
Blade-Element Parameters . . . . .	5
RESULTS AND DISCUSSION . . . . .	7
Visual Studies . . . . .	8
Noncavitating Performance . . . . .	9
Overall performance . . . . .	9
Inlet conditions . . . . .	10
Outlet flow conditions . . . . .	11
Cavitation Performance . . . . .	13
Overall performance . . . . .	13
Radial distributions . . . . .	15
Radial Equilibrium . . . . .	17
Cavitation Damage . . . . .	17
REMARKS . . . . .	18
SUMMARY OF RESULTS . . . . .	18
APPENDIXES	
A - SYMBOLS . . . . .	20
B - EQUATIONS . . . . .	22
C - EFFECT OF MASS-FLOW REDISTRIBUTIONS ON DEVIATION ANGLE . . . . .	25
REFERENCES . . . . .	26
TABLE . . . . .	27
FIGURES . . . . .	28



NATIONAL AERONAUTICS AND SPACE ADMINISTRATION

---

TECHNICAL NOTE D-1170

---

INVESTIGATION OF THE PERFORMANCE OF A 78°

FLAT-PLATE HELICAL INDUCER

By Richard F. Soltis, Douglas A. Anderson,  
and Donald M. Sandercock

SUMMARY

The coupling of a cavitating inducer with a pump, in order to realize the advantages of higher mechanical speeds, has found wide use in missile applications. An effective and quite easily fabricated blade shape employed in the inducer has been the flat-plate helix. This report presents the measured performance of an inducer of this type. The rotor, 5 inches in diameter, consisted of three blades with a hub-tip ratio of 0.5 and a helix angle of 78° at the tip. All tests were made in water.

Performance results over a range of flows are presented at both cavitating and noncavitating conditions. This includes both the overall performance and radial distributions of flow conditions and selected blade-element performance parameters. In addition, photographs that visually describe flow conditions at various modes of operation are presented. A comparison of the measured axial velocity distributions with those computed assuming simple radial equilibrium provides a check on the validity of the radial equilibrium assumption.

INTRODUCTION

The constant challenge to obtain minimum size and weight of the turbopump for missile application has resulted in continued compromises in pump design. Since the pump weight is strongly dependent on rotative speed, increased operating speeds are suggested. Unfortunately, the freedom in the selection of pump speeds is limited by the deleterious effects of cavitation both on pump performance and in causing mechanical damage to the pump.

A conventional parameter used to relate rotative speed and suction head requirements is the suction specific speed, defined as

$$S = \frac{NQ^{1/2}}{H_{sv}^{3/4}} \quad (1)$$

All symbols are defined in appendix A. Reference 1 notes how improvement in the suction characteristics of a pump is reflected in decreased weight of the complete powerplant.

A more promising method of increasing the suction characteristics of the pump is the cavitating inducer located upstream of the main pump. The function of this inducer is to operate with some cavitation and to add sufficient head to the fluid to recompress the vapor and prevent the occurrence of cavitation in the main pump. With the trend toward higher suction speed pumps, the cavitating inducer has found wide use. Although many design geometries exist, inducers are generally helical in shape, employ high solidity, and have a small number of blades and a high blade angle (used herein as the angle between the blade meanline and the axial direction). References 1 and 2 discuss the function of the inducer and show, in a qualitative sense, the general flow patterns that may be expected in an inducer in various stages of cavitation. In both cases, the inducers were operated in cold water.

This report presents the performance of a flat-plate helical inducer (constant lead) with a blade angle of  $78^\circ$  at the tip. The data presented include overall performance and radial distributions of flow conditions and selected blade-element performance parameters for both cavitating and noncavitating conditions. Shown also is an investigation of the validity of the simple radial equilibrium expression,

$$\frac{\partial h}{\partial r} = \frac{V_\theta^2}{gr} \quad (2)$$

under the various modes of operation.

To date, inducer investigations have been primarily concerned with the overall performance supplemented by photographs and visual observations during cavitation. The investigations cover a range of blade geometry (solidity, helix angle, hub-tip radius ratio, etc.) as well as a range of flow conditions (net positive suction head, flow coefficient, etc.). The radial distributions of flow conditions, as presented in this report, provide a further step toward the understanding of the flow through an inducer. This type of information is necessary in the prediction of radial distribution of velocity diagrams and head rise that a succeeding rotor must accept.

## APPARATUS AND PROCEDURE

### Test Rotor

The rotor used for the investigation reported herein is the simplest type of cavitating inducer to construct. The blade shape is a helical surface with a tip blade angle of  $78^\circ$ . The rotor tip diameter was 4.956 inches, and the hub diameter was 2.478 inches. Both hub and tip diameters were maintained constant through the inducer. The rotor had three blades with a linear variation of blade thickness from 0.10 inch at the tip to 0.19 inch at the hub. Tip solidity was 1.856. Significant geometric features of this rotor are listed in table I.

The rotor was machined from the 400-series stainless steel. Both the leading and trailing edges were sharpened to a wedge shape symmetrical about the blade centerline. A photograph of the rotor is shown in figure 1.

### Test Facility

This investigation was conducted in the Lewis Water Tunnel, a closed-loop-pump test facility. (This is the same system described in ref. 3, but with a different test section, drive motor, and gearbox.) Figure 2(a) presents a schematic diagram of the test setup, while figure 2(b) is an actual photograph of the facility; a detailed description is contained in reference 3. The filter was capable of removing particles of 5 microns or larger. The air content of the water was measured by means of a blood gas analyzer.

The test rotor was powered by a 3000-horsepower variable-frequency motor through a suitable gear box. The upper half of the casing enclosing the test section was made of a transparent plastic suitable for observing and photographing cavitation phenomena throughout the rotor. Figure 3 is a photograph of the test section showing the rotor mounted in place, transparent casing, probe actuators, and pressure transducers.

### Instrumentation

The detailed rotor performance was obtained from radial surveys of the flow conditions approximately 1 inch upstream of the inducer leading edge and 1 inch downstream of the inducer trailing edge, as shown in figure 4. At both radial locations, total and static pressures and flow angles were measured at seven programed radial positions. The total-pressure claw (measures total pressure and angle) and the static-pressure wedge probes are shown in figure 5. Direction-sensing elements automatically aligned the probes with the local flow direction. Zero angles of

both total and static probes and calibration of the static-pressure probes were determined in an air tunnel. All pressures were measured with transducers and were recorded, along with angle measurements, on paper tape through an automatic digital potentiometer.

The temperature of the water in the test loop was measured with a thermocouple. The flow rate was obtained from pressure measurements across a Venturi flowmeter. Pump speed was measured by means of an electronic tachometer used in conjunction with a magnetic pickup on the rotor shaft.

Differential pressures were measured wherever possible to allow smaller range pressure transducers to be used. Hence, measurement accuracy was increased, as all transducers had a maximum error of 0.5 percent of full scale, and a compounding of errors in the calculations was avoided. The estimated maximum measurement errors were:

Inlet total pressure, $P_1$ , lb/sq in. . . . .	$\pm 0.25$
Inlet dynamic velocity head, $P_1 - p_1$ , lb/sq in. . . . .	$\pm 0.075$
Head rise across inducer, $\Delta P$ , lb/sq in. . . . .	$\pm 1.75$
Outlet dynamic velocity head, $P_2 - p_2$ , lb/sq in. . . . .	$\pm 0.25$
Angle, deg . . . . .	$\pm 0.50$
Rotor speed, rpm . . . . .	$\pm 20$
Venturi flow, percent . . . . .	$\pm 1.0$

#### Procedure

All operations of the inducer were conducted with a constant water temperature of 80° F and an air content less than 3 parts per million by weight. At each data point, the inlet pressure, the flow rate, and the rotor speed were held constant while data were taken at the seven radial positions from hub to tip. One complete point (all seven radial positions) took about 10 minutes of running time on the digital unit. Data were taken in groups of constant inlet pressure and shaft speed, while the flow rate was varied from the open throttle condition to a point where excessive rig vibrations were encountered. (As the inlet pressure could not be set below atmospheric, the rotor speed was increased to obtain higher suction speed conditions at the rotor inlet.)

To supplement the measured performance results, photographs of the flow across the inlet portion of the blades were taken, particularly of the flow in a cavitating environment. Photographs were recorded on 16-millimeter film with a synchronized camera and light source at a frame rate of approximately 24 frames per second. The light source was triggered by a magnetic pickup on the rotor shaft, and the duration of flash was between 1 and 2 microseconds.



## Calculations

The equations used to calculate the inducer overall performance, as well as the performance across selected blade elements, are presented in appendix B.

Some measure of the reliability of the data may be obtained from figures 6(a) and (b), which compare the integrated weight flows at the inducer inlet and outlet measuring stations, respectively, with the flow measured by the Venturi meter. At the rotor inlet the integrated flows compare quite favorably with the measured Venturi flows, with a maximum error of 6 percent and with the majority of comparisons within 3 percent. At the exit measuring station, the comparisons are not as favorable, with a maximum difference of 17 percent but the majority within 10 percent.

Some factors that probably contribute in some degree to the difficulty of obtaining accurate integrated flows at the inducer outlet include:

(1) Increased sources of disturbance (compared with noncavitating flow) to the fluid originating from the cavitating portions of the blade. This cause is partially borne out by the results shown in figure 6(b), which indicate that, in general, as  $H_{SV}$  is lowered (intensity of cavitation increased), the differences between the integrated and measured flows increase.

(2) Tacit assumption that a single-point measurement at a given radius represents an average value of any circumferential variation at that radius.

(3) Cavitation occurring on probes at low inlet pressures. Cavitation in the flow around the probes at the inlet measuring station has been observed. Although the probes at the exit measuring station could not be seen, at test points where the head rise across the inducer is relatively small, the possibility of cavitation on the probes still exists.

(4) Measurements at low flows indicating the existence of reverse flow regions near the hub at the rotor exit. Inconsistencies in the calculated performance parameters involving static-pressure measurements in, and near, these regions have been observed.

## Blade-Element Parameters

The presentation and analysis of data follow a blade-element approach, that is, a belief that the blade-row overall performance can be

described by a summing-up of the performance occurring across individual blade elements along the radius. The first requirement is the definition of a blade element. A general definition for a blade element is that it lies along a surface of revolution generated by a streamline; the definition is usually simplified by assuming the streamline to occur across the blade in a straight line. Furthermore, to alleviate complications in the data-taking and computing procedures, this definition of a blade element is assumed to apply under all operating conditions. For simplicity, then, a blade element as used herein is assumed to lie along a cylindrical surface. It is recognized, however, that, as mass-flow shifts occur across the blade row, the assumed blade elements will deviate increased amounts from streamline flow. The following brief discussion of the selected blade-element performance parameters and their interdependency may aid in interpreting the curves and analysis to be presented.

The performance parameter of primary interest is the head rise coefficient  $\psi$  across the inducer. The inducer must provide sufficient pressure rise so that the succeeding main pump or pump stages can perform in a cavitation-free environment. Of secondary importance, in most cases, is the efficiency at which the inducer head rise is produced.

The head rise and efficiency depend on the energy added to the fluid by the rotor (ideal head rise coefficient)  $\psi_i$  and the losses incurred in the process. The loss across a blade element is reported as a relative total-pressure loss coefficient  $\bar{\omega}$ , as defined by equation (B5). The ideal head rise (eq. (B2)) for the condition of no inlet whirl is computed from the outlet velocity diagrams. The outlet tangential velocity used in the calculation of ideal head rise is, in turn, affected by the amount of turning done by the blade and the axial velocity. The fluid turning is studied by means of deviation angle, which is related to the fluid turning for a helical blade through the equation

$$\Delta\beta' = i - \delta \quad (3)$$

Axial velocity distribution must satisfy both continuity and the radial equilibrium requirements. Both deviation angle and axial velocity distributions are influenced, in turn, by the magnitude and distribution of loss.

Accordingly, the flow and element performance parameters selected for presentation include:

- (1) Head rise coefficient,  $\psi$
- (2) Efficiency,  $\eta$

- (3) Relative total-pressure loss coefficient,  $\bar{\omega}$
- (4) Ideal head rise coefficient,  $\psi_i$
- (5) Deviation angle,  $\delta$
- (6) Outlet flow coefficient,  $\psi_2$
- (7) Inlet flow coefficient,  $\psi_1$
- (8) Static-pressure rise coefficient,  $\psi_s$

When the measured radial distributions of these parameters are examined, the relative sensitivity of performance to changes in these parameters at the various radial locations should be kept in mind. For instance, typical velocity diagrams for this rotor show that the effect of the same change in axial velocity or deviation angle on ideal head rise is approximately 10 times as great at the tip element as at the hub element.

The complete outlet velocity diagram may be reproduced from the flow coefficient, deviation angle, and blade speed by using the following relations:

$$\beta' = \gamma + \delta \quad (4)$$

where, for a flat-plate helical inducer,

$$\tan \gamma = \frac{r}{r_t} \tan \gamma_t \quad (5)$$

If it is desired to compare the measured trends with predicted theoretical variations, reference 4 may be utilized. Reference 4 presents the effects of varying certain geometry features (helix angle, hub-tip ratio, hub and tip taper, etc.) and flow parameters (loss coefficient, deviation angle, flow coefficient, etc.) on the radial distributions of head rise, axial velocity, and efficiency for the flat-plate helical inducer.

## RESULTS AND DISCUSSION

In order to facilitate the presentation, the noncavitating and cavitating performance is presented and discussed in separate sections. Since the details of the data are presented by the figures, the discussion points out only the important trends.

As mentioned earlier, to aid in visualizing the flow, photographs of the flow over the inlet portion of the blades were taken at various modes of operation. These and some visual observations made during the tests are presented first.

### Visual Studies

A typical performance curve such as shown in figure 7, where flow coefficient (hence, inlet flow conditions) is maintained constant while  $H_{SV}$  (or  $k$ ) is systematically reduced, is a common method of presenting cavitation performance. Operation is generally initiated at some high inlet pressure where the blade operates in a cavitation-free environment. Inlet pressure is then reduced until first visible signs of vaporization occur. Further decreases in inlet pressure result in increased amounts of vapor formed. Thus, cavitation development is divided into several distinct stages. These include (in order of appearance as the  $H_{SV}$  is reduced): (1) cavitation inception, (2) unsteady cavitation, and (3) cavitation breakdown.

"Cavitation inception" as applied to visual observations implies the first appearance of cavitation. (As applied to measured performance results, cavitation inception usually refers to the initial dropoff in performance due to cavitation.) The first cavitation is usually observed in the blade-tip region and may occur at relatively high values of  $H_{SV}$ . This is cavitation occurring in the core of the tip vortex resulting from the blade-tip clearance flows (see ref. 5). Depending on the operating condition, the cavitation extends various distances ahead of the blade. The photographs in figure 8 are examples of the blade-tip vortex cavitation (at relatively high  $H_{SV}$  values) showing the cavitating vortex moving increasing distances into the inlet passage as flow coefficient is decreased (blade loading increased). (Figure 7 gives location of photos on performance curve.) Small amounts of blade surface cavitation are also occurring on these photos as a sheet with streamers attached to the leading edge. Reference 6, however, indicates that, in general, the head generated by the rotor does not suffer until this cavitation region extends to the leading edges of adjacent blades.

Figure 9 gives an example of the "unsteady cavitation" region, which occurs at a lower  $H_{SV}$  than the "cavitation inception" region. For these film strips, the blade speed and camera framing rate combine such that each successive picture in a sequence shows the same blade of the three-bladed rotor in the same position either six or seven revolutions later.

The sequence of photographs taken at this operating condition characteristically shows a blade passage containing large amounts of cavitation in one picture and the same passage relatively free of cavitation

in a succeeding picture. Although the relative amount of cavitation occurring in a blade passage is most easily distinguished by the occurrence or absence of the tip vortex cavitation, the blade surface cavitation follows a similar pattern; that is, if the tip vortex grows, the surface cavitation grows; if the tip vortex declines, the surface cavitation also declines. When projected on a screen, it cannot be distinguished whether the cavitation zones are moving from one blade passage to the next (rotating cavitation) or are moving back and forth in the same passage in a pulsating motion. It was also observed during operation in this flow regime that the axial clearance space (see fig. 4) between the rotor and stationary inlet hub fairing fluctuates. This could be an indication of a rapid variation (or redistribution) of blade forces, and, consequently, head produced by the inducer. These fluctuations in axial clearance space were not observed at other operating conditions, either cavitating or noncavitating.

As the inlet pressure (net positive suction head) is further reduced from the "unsteady cavitation" region, the "cavitation breakdown region," where each reduction in  $H_{sv}$  results in a significant drop in head rise produced by the inducer, is reached. Cavitation is steady and appears in all passages, as depicted in figure 10. In all other photographs that fall in, or close to, this region both the tip vortex and blade cavitation extend increasing distances along the blade passage as  $H_{sv}$  is successively lowered. Blade cavitation at all conditions was characterized by a sheet or streamers (or both) starting at the leading edge and lying along the blade suction surface. It should be noted that the inducer head rise shown in figure 7 is obtained from a single probe located very close to the middle of the annulus both upstream and downstream of the rotor ( $r = 1.865$  in.).

#### Noncavitating Performance

Overall performance. - Figure 11 presents the overall performance of the inducer in terms of head coefficient  $\psi$ , flow coefficient  $\phi$ , and efficiency  $\eta$ . The head flow characteristic line is composed of data obtained at net positive suction head values of 114 and 85 feet. The performance curve shows the usual inverse relation between flow and head rise generally associated with the axial-flow type of pump. Head coefficient and efficiency were obtained by mass-averaging measurements gathered from radial surveys.

Over the range of flow investigated, the overall efficiency remained in a range of 0.80 to 0.82 except at the high flow ( $\phi > 0.15$ ), where some slight dropoff is evidenced.

Figure 12 compares the overall noncavitating performance obtained from the inducer reported herein with the results of a flat-plate inducer

with the same helix angle reported in reference 2. The table in this figure presents a comparison of significant geometry features and operating speed of the two rotors. Principal differences in the two investigations are the size of the rotors and the methods of measuring pump head rise. The head rise of reference 2 was obtained from a single measurement taken at midpassage and, as noted in reference 2, is probably conservative. The pump head rise reported for this investigation represents a mass-averaged value as obtained from radial surveys. For comparison, the head rise measured at the mean passage station for this investigation is included. At the lower flow, the differences in measuring techniques appear to account for the differences noted in the two investigations; however, at the high flow, other factors are necessary to explain the differences.

A check of all the radial distributions of measured head coefficient presented herein was made to determine at what radius the element head coefficient equaled the mass-averaged value. Interestingly enough, at all operating conditions, the radius at which  $\psi_r$  equaled  $\bar{\psi}$  was approximately 2.20 inches. This value represents approximately 88 percent of the rotor tip radius or 24.3 percent of the passage height from the tip inward.

A similar impasse exists in a comparison of efficiencies. The maximum efficiency reported in reference 2 (0.73 at  $\phi = 0.12$ ) was 8 to 10 points lower than the best efficiency observed in this investigation. In calculating efficiency, a knowledge of the input power to the rotor is required (eq. (B8)). The different techniques for obtaining this value used in the two investigations further complicate a comparison of inducer performance.

Inlet conditions. - Figure 13 presents the radial distributions of incidence angle, flow angle, flow coefficient, and inlet total head for three flow coefficients encompassing the range of noncavitating operation. In the inlet region it is assumed in the calculation of velocity diagrams that there is no inlet whirl ( $V_{\theta,1} = 0$ ). This, in effect, credits all changes in flow to the rotor. The validity of this assumption can be assessed from angle measurements which indicated that the absolute inlet flow angle was small ( $\lesssim 3^\circ$ ) for most cases. For an axial velocity of 30 feet per second, a  $3^\circ$  inlet flow angle would affect the incidence angle by approximately  $0.07^\circ$  at the tip and  $0.26^\circ$  at the hub and the magnitude of axial velocity by less than 1 percent. Exceptions to this limit were noted in the tip region for the minimum-flow test points for each of the  $(H_{5V})_N$  characteristic curves. These operating points are also characterized by a decrease of axial velocity in the tip region. The two parameters show a qualitative relation in that the inlet flow angle increases as the axial velocity decreases. For the low-flow coefficient

point presented in figure 13 inlet flow angles of approximately  $10^\circ$  were observed in the tip region. At all other radial positions the flow angles were within the established limit.

At the high and midrange flow coefficients, the slight decrease in axial velocity from hub to tip is probably that required by the curvature of the hub inlet fairing. The only change is the level of velocity which reflects the lower flow; that is, the same profile exists, but at a lower level. At these operating points the inlet total head is essentially constant across the passage with no evidence of hub or tip wall (casing) boundary-layer effects. Other test points at similar inlet conditions did indicate very slight decreases in total pressure at the radial measuring position located at  $r = 2.42$  inches (approx. 5 percent of the passage height from the tip), but no dropoff was noted in the hub region. In all cases the wall boundary layers at the inlet are evidently very small and should have little influence on the blade performance.

At the lowest flow coefficient, significant redistributions of flow have taken place. Both axial velocity and total head display sharp decreases from the mean to the tip regions with the possibility of a reverse-flow region occurring in the tip region. At low flow coefficients, reference 2 also noted a reversal of the inlet flow in the tip region by visual observation of tufts mounted on the outer casing.

References 7 and 8 indicate that the influence of the rotor vanes on the meridional flow in front of the vane system is such that decreased meridional velocities and the possibility of reversed flow occur in the tip region. Another source of disturbance to the inlet flow may be related to the strong tip clearance flows observed at the leading edge for this mode of operation. Photographs taken at low flow operation (high blade loading) show cavitation in the tip vortex extending into the inlet flow passage (see fig. 8(b)). Blockage effects of this disturbance could cause a redistribution of inlet mass flow similar to the observed distribution. And, finally, the influence of secondary flows on the inlet flow distribution is relatively unknown. It has been estimated (seminar notes at Pennsylvania State Univ., summer of 1958) that the quantity of radial boundary-layer flows in an inducer is significantly (one or two orders of magnitude) larger than that experienced in axial-flow compressor rotors. If this estimate is correct, some information on this type of flow may be necessary before the true inducer flow patterns can be understood.

Outlet flow conditions. - Figure 14 shows the radial distributions of blade outlet flow conditions and selected blade-element parameters for the high-flow, midflow, and low-flow ranges.

At all flow coefficients a gradient of head rise from hub to tip is noted, a distribution typical for the flat-plate helical inducer.

As the mode of operation changed toward lower flow coefficients, both the level of head rise and the gradient from hub to tip are increased. The latter trend is indicated analytically in reference 4 in the relative effect of a change of axial velocity on the ideal head rise at the various radial locations.

For the case of no inlet whirl ( $V_{\theta,1} = 0$ ) the ideal head rise coefficient at any given radial location is dependent on the outlet relative flow angle and the outlet flow coefficient, as noted by the equation

$$\psi_i = \frac{U_2 V_{\theta,2}}{U_t^2} = \left(\frac{r}{r_t}\right)^2 - \left(\frac{r}{r_t}\right) \phi_2 \tan \beta_2' \quad (6)$$

In the discussion of the data, the effects of these two parameters on pump performance are generally considered together, since it is difficult to find examples to demonstrate individual effects.

In this report the relative outlet flow angle is discussed in terms of deviation angle, which is related to the blade-outlet angle and outlet relative flow angle by equation (B7). From equation (B7) it can be seen that deviation angle serves as a measure of the departure of the flow from that associated with perfect guidance by the blades. The assumption of perfect guidance of the flow is one often used in theoretical calculations of inducer performance. Of special interest are the negative values of deviation angle noted both for the noncavitating (fig. 14) and cavitating operation (fig. 18). A study of the flow conditions at which negative deviation angles are calculated points out that they occur only during operation when the radial distributions of axial velocity at the blade inlet and outlet measuring stations indicate that sizable mass-flow shifts are occurring across the inducer. A calculation was made to determine whether the streamline curvature between the blade trailing edge and the outlet measuring station (located approximately 1 in. downstream of the rotor trailing edge) could account for the negative values. In brief, the calculation attempted to construct the velocity diagrams occurring at the blade trailing edge from those computed by measurements obtained at the exit measuring station. The procedure used and the results obtained are presented in appendix C.

Based on the results of appendix C, it appears probable that the negative deviation angles are a result of the location of the discharge measuring station rather than some flow phenomena. It is also noted that negative deviation angles are not computed at the higher flow coefficients where the mass-flow shifts are not indicated. Of course, the higher flow conditions also represent different loading distributions on the blades.



At the low flows the static head gradient requirements become so large that the axial velocity goes to zero in the vicinity of the hub. This trend has been pointed out in the analytical studies reported in reference 4, which also graphically shows the effect of losses on the axial velocity distribution. Observation of tufts mounted on the hub downstream of the inducer in reference 2 show noticeable backflows occurring at low flow coefficients with the compensating radial outflows. Reference 2 indicates that the flow on the hub appears to separate about halfway through the impeller.

At all flow coefficients, the radial distributions of loss in figure 14 appear similar in trend, with a sharp increase from the mean to the tip and smaller (if any) increases from the mean to the hub. Only in the tip region does any consistent trend of loss with inlet flow coefficient (incidence angle) appear. As the inlet flow coefficient is decreased (increasing incidence angle and blade loading), the loss coefficient increases. A check on the efficiency values in this region shows that, even though the losses increased, the increase in energy addition occurred at an even faster rate with resulting increases in efficiency. This example points up the fact that efficiency is a function of both loss and energy addition.

In general, the radial efficiency distribution is the inverse of the loss variation. The sharp increase in loss coefficient measured in the inducer tip region under all operating conditions is interpreted as an indication that secondary flow losses, including the radial transport of low-energy blade boundary-layer fluid into the tip region in an inducer rather than a profile-type loss, probably determine the radial distribution for this type of rotor.

#### Cavitation Performance

Overall performance. - The overall cavitation performance is presented in figure 15. For comparative purposes, the noncavitating data are also included. The data are shown as mass-averaged values of head rise coefficient  $\bar{\psi}$  and efficiency  $\bar{\eta}$  expressed as functions of flow coefficient  $\bar{\phi}$  at constant values of  $(H_{SV})_N$ . Although the cavitating performance data were obtained at various rotor speeds as indicated by the table in this figure, all  $H_{SV}$  values shown have been normalized by the tip speed to an equivalent value for 9000-rpm operation. In all cases the performance curves were terminated when severe rig vibrations were encountered. It is recognized that a locus of such terminal points might then represent a "stall" limiting curve for this inducer. However, at this time no attempt is made to identify any limiting conditions: first, because the data indicate that the rotor speed affects the location of the terminal points; and, secondly, since the dynamics of the system must affect the stall point, consequently any stall line defined

here would be peculiar to this particular system only. For these reasons no generalizations are attempted herein.

Evidence of a speed effect on the cavitating performance is indicated by comparing the performance at  $N = 9000$  rpm and  $(H_{sv})_N = 33.8$  feet with that at  $N = 10,500$  rpm and  $(H_{sv})_N = 32.3$  feet (recall that both  $(H_{sv})_N$  values are normalized to a speed of 9000 rpm). The performance at  $(H_{sv})_N = 32.3$  feet is slightly improved over that obtained at a higher net positive suction head ( $(H_{sv})_N = 33.8$  ft) at all modes of operation and shows an increased range of operation. Note also that the efficiency is higher at all flow coefficients for the curve at  $(H_{sv})_N = 32.3$  feet. Since both the speed and  $(H_{sv})_N$  were changed, the relative effects of the changes in the two variables could not be evaluated at this time. However, it serves to demonstrate scale effects in regard to a change in speed. It may further be speculated that, if operation at  $(H_{sv})_N$  values less than 32.3 feet could have been conducted at a speed of 9000 rpm, a larger falloff in performance would have resulted than was experienced at the higher rotative speeds.

E-1368

A more general method of presenting cavitation data is in terms of the cavitation number  $k$ , defined as

$$k = \frac{h_l - h_v}{V_1^2 / 2g} \quad (7)$$

which is equivalent to (assuming  $V_{\theta,1} = 0$ )

$$k = \frac{2gH_{sv}}{U_t^2 \left[ \left( \frac{r}{r_t} \right)^2 + \phi^2 \right]} - \frac{\phi^2}{\left( \frac{r}{r_t} \right)^2 + \phi^2} \quad (7a)$$

Equations (7) and (7a) represent local values of cavitation number as would be applied to any blade element. When referring to an overall blade cavitation number, a form of equation (7a) using blade-tip speed  $U_t$  and an average flow coefficient  $\phi_1$ , obtained from the measured flow and inlet geometric area, is used. This cavitation number is designated as  $k$ .

Figure 16 shows the dropoff of head rise coefficient with cavitation number while flow coefficient is kept constant. The curves of this figure were obtained by interpolating the data of figure 15. Even though

the symbols in figure 16 represent interpolated values of the curves of figure 15, for most cases they are very close to actual test points. For orientation of the data with respect to suction specific speed, constant values of this parameter are also shown. The cavitating performance data lie in a suction specific speed range of 20,000 to 26,000.

The data obtained in this investigation do not clearly define the cavitation inception point which, when interpreting performance results, is usually defined as the point where the head rise drops off from the noncavitating value by 1 or 2 percent. Consequently, some liberty may have been taken in drawing the curves in this general area.

The  $\bar{k}$  values at which cavitation breakdown occurs are reasonably well defined. (Cavitation breakdown is defined as the point where a further drop in  $H_{SV}$ , or  $\bar{k}$ , results in a large drop in head rise.) Figure 16 indicates that this occurs at a  $\bar{k}$  value on the order of 0.035, which is comparable with suction specific speeds of approximately 23,000. These values compare favorably with those obtained in reference 2. This region would be the probable operating region for a high-suction speed inducer when used in conjunction with a centrifugal impeller or a number of high-pressure axial-flow pump stages in either a chemical or nuclear rocket application. The usual design stipulation of an allowable decrease of 1 or 2 percent in overall pump head rise from the noncavitating value usually results in the inducer operating at a considerably lower percentage of its own head rise level.

Figure 17 presents a composite of the results of figure 16. In this figure, the head rise coefficient expressed as a ratio of the noncavitating value is plotted against the cavitation number  $\bar{k}$ . The symbols represent actual test points presented in figure 15.

Radial distributions. - In order to examine blade operation under varying degrees of cavitation, figures 18(a) to (g) present radial distributions of selected flow and blade-element performance parameters for a constant flow coefficient and varying values of  $(H_{SV})_N$ . Since this comparison requires actual test-point data, overall performance levels of the points utilized are listed in order that they may be identified with the overall results of figure 15. The average inlet flow coefficients are approximately the same. The interrelations between the various flow and element performance parameters have already been discussed; hence, this section is primarily concerned with the effects of varying degrees of cavitation on the radial distributions.

An examination of the data for consistency of the flow and performance parameters under cavitating conditions indicated the following:

(1) Head rise coefficients and flow angles showed consistent trends at all operating conditions. This would indicate satisfactory total-pressure and angle measurements.

(2) At certain low  $H_{SV}$  (or  $k$ ) operation and in the hub region where no-flow or backflow regions occur (as indicated by zero axial velocities), large variations and certain inconsistencies in the radial distributions of flow and performance parameters are indicated. Causes for these discrepancies probably lie in the occurrence of cavitation on the wedge-type static probe itself and in the difficulty of obtaining good static-pressure measurements in the eddy-type flows occurring in this separated region on the hub. These factors must be weighed in any interpretation of the data.

At a given flow coefficient, the radial distribution of head coefficient under varying degrees of cavitating conditions has the same shape as that measured for the noncavitating mode of operation, but the magnitude varies with  $H_{SV}$  (degree of cavitation). As the flow coefficient is decreased and the head rise gradient increases, the absolute change in head coefficient varies from hub to tip. However, the percentage decrease remains roughly the same along the radius.

The energy input distributions show results similar to the head coefficient variations. As the  $(H_{SV})_N$  is decreased, the radial variation of  $\psi_i$  is similar to the noncavitating values, but at a lower magnitude.

In general, as cavitation increases, the deviation angle increases - this is in the direction of decreasing the turning angle and, for a given axial velocity, the outlet tangential velocity.

The general trend of loss coefficient is to increase as  $(H_{SV})_N$  decreases (degree of cavitation increases), especially from the mean to tip radius, although the scatter of the data tends to obscure this observation.

The effect of cavitation on the axial velocity distributions is to decrease the steep gradients obtained under noncavitating conditions. As the radial equilibrium requirements become less severe, the axial velocity gradients are, in turn, also relaxed. Intermingled with the preceding are the effects of any mass-flow redistributions that take place because of physical blockage of the flow by cavitation.

It is notable also that, as the blade-exit axial velocity gradients flatten out, the steep gradients of axial velocity measured at the blade inlet also disappear. This would indicate that the low inlet axial velocity in the tip region is primarily a result of the action of the vanes on the inlet meridional flows.

One additional blade-element parameter, a static-pressure head rise coefficient  $\psi_s$ , is presented with the cavitation performance. This is shown, since it is the additional static-pressure head that is needed to

suppress cavitation in succeeding rotor rows. The static head rise distributions generally follow the radial variations of total head rise, while the ratio of static head rise to total head rise falls roughly in the range of 0.65 to 0.75 in the tip region and 0.85 to 0.95 in the hub region.

### Radial Equilibrium

The solution of the equations governing the fluid flow to obtain the velocity diagrams at any particular station requires an expression for the radial pressure gradient (radial component of equation of motion). The form generally used in pump design is

$$\frac{\partial h}{\partial r} = \frac{v_\theta^2}{gr} \quad (2)$$

which equates the radial static head gradient to the whirling motion of the fluid and neglects any effect due to radial motion of the fluid. Figure 19 presents a comparison of the distributions of measured axial velocities with those computed using the measured values of total pressure and angle in equation (2). The points shown cover a range of operating conditions for both cavitating and noncavitating flow. The good correlation between the computed and measured axial velocities indicates that equation (2) may be applied to the flow behind this type of inducer under all operating conditions. Reference 9 discusses the use of various forms of the radial equilibrium equation in detail.

### Cavitation Damage

As a point of interest, photographs showing a closeup view (fig. 20) and the location (fig. 21) of cavitation damage noted on the blade surfaces at the conclusion of the tests are presented. For the type of test procedure utilized herein, involving radial surveys of the flow annulus, the inducer is required to operate in a cavitating condition for relatively long periods of time. During these tests, no attempt was made to monitor the cavitation damage with respect to time or intensity of cavitation encountered. Tests made after data-taking was concluded showed that cavitation damage had no measurable effect on performance.

Figure 21 shows the location of cavitation damage on the suction surface of the blade. A similar zone was located on the pressure surface at the outlet of each blade passage (immediately downstream of trailing edge of the adjacent blade) and at a radius of approximately 2 inches. The principal damage area extended about  $1\frac{1}{2}$  inches along the blade and varied from 0.1 to 0.2 inch in width.

## REMARKS

Recently, increased interest in the study of cavities in cascades of flat plates has been indicated. Theoretical solutions involving free streamline theory and linearized cascade theory have been attempted. Reference 10 outlines a number of methods used and also correlates the results calculated from the essentially two-dimensional theory with measurements obtained in the three-dimensional atmosphere of the flat-plate inducer. Although the results show promise, significant deviations between the theoretical and test results have been noted. The additional effects of operating in a three-dimensional environment (radial varying blade angles, three-dimensional flows, losses, etc.) require further investigation. Data such as obtained in this investigation are necessary to assess the magnitude of this type of effects.

E-1368

## SUMMARY OF RESULTS

The performance of a three-blade 5-inch-diameter flat-plate helical inducer with a helix angle of  $78^\circ$  (angle between a tangent to the blade and the axial direction) at the blade tip was investigated. The data presented include performance results obtained from radial surveys of flow conditions at the rotor inlet and outlet as well as photographs of the flow across the rotor at various operating conditions.

Visual studies of the flow indicated:

1. Some cavitation on the blade surface and in the tip vortex (resulting from blade tip clearance flows) exists before any dropoff in measured head rise is observed.

2. As the inlet flow coefficient is decreased, the tip vortex stands out increasing distances into the inlet flow region. This extension of the tip vortex is suggested as a possible source of disturbance to the inlet flow.

3. In the region where the initial dropoff of head rise due to cavitation is measured, an unsteady type of cavitation was photographed. However, what these instabilities represented in terms of quantitative measurements of variations in flow or head rise could not be determined with the present instrumentation.

The noncavitating performance showed:

1. A nearly linear relation between the overall head rise coefficient  $\bar{\psi}$  and overall flow coefficient  $\bar{\phi}$  with a maximum  $\bar{\psi}$  of 0.179 obtained at the minimum  $\bar{\phi}$  of 0.11.

2. A maximum efficiency of approximately 0.82 and an efficiency of 0.80 or greater over about 75 percent of the range covered.

3. At lowest flow, the radial distribution of inlet flow coefficient displayed a sharp decrease from the mean to the tip regions, which indicated the probable existence of reverse-flow regions in this operating regime. Inlet total head shows a similar radial distribution. Some sources of disturbance to the inlet flow are indicated but could not be evaluated at this time.

4. A radial gradient of head rise coefficient at all flows with the highest values at the blade tip. The gradient increased as the flow decreased.

5. A very sharp increase in loss coefficient from the mean to the tip region that was typical for all operating conditions. It is probable that losses associated with secondary flows (in particular, the radial transport of rotor blade boundary layer) assume a position of importance for this inducer type blade.

6. As flow is decreased, the radial equilibrium requirements at the blade outlet change until at some operating condition zero axial velocities (reverse flows) are measured in the hub region.

The effects of cavitation as indicated by the cavitation performance results were:

1. Cavitation breakdown occurs at a  $\bar{k}$  value of approximately 0.035 (suction specific speed  $\approx 23,000$ ) for this rotor configuration.

2. The measured performance at  $(H_{sv})_N = 33.8$  and 32.3 feet and  $N = 9000$  and 10,500 rpm, respectively, indicates that the cavitating performance of this rotor is affected by blade speed.

3. The decrease in head rise coefficient  $\psi$  as  $(H_{sv})_N$  is lowered occurs at all radii and by approximately the same percentage. This adverse effect on head rise coefficient results from a general decrease in ideal head rise coefficient  $\psi_i$  and increase in loss coefficient  $\omega$  as the degree of cavitation increases.

The close correlation between measured radial distributions of axial velocity and those computed assuming simple radial equilibrium demonstrates the validity of the latter assumption under all flow conditions investigated.

Lewis Research Center

National Aeronautics and Space Administration

## APPENDIX A

## SYMBOLS

$g$	acceleration due to gravity, 32.17 ft/sec <sup>2</sup>
$H$	total head, ft
$H_{SV}$	net positive suction head, $H_{SV} = H_1 - h_v$
$h$	static head, ft
$h_v$	vapor pressure, ft
$i$	incidence angle, deg
$k$	cavitation number, $k = \frac{h_1 - h_v}{V_1^2/2g}$
$N$	rotative speed, rpm
$P$	total pressure, lb/sq in.
$p$	static pressure, lb/sq in.
$Q$	flow rate, gal/min
$r$	radius, ft
$S$	suction specific speed, $S = \frac{N\sqrt{Q}}{(H_{SV})^{3/4}}$
$U$	rotor speed, ft/sec
$V$	fluid velocity, ft/sec
$\beta$	fluid angle, angle between fluid velocity and axial direction, deg
$\gamma$	blade angle, angle between tangent to blade mean camber line and axial direction, deg
$\delta$	deviation angle, deg



$\eta$  efficiency  
 $\phi$  flow coefficient  
 $\psi$  head coefficient  
 $\bar{\omega}$  relative total-pressure loss coefficient

Subscripts:

$h$  hub  
 $i$  ideal  
 $m$  measured  
 $N$  normalized  
 $s$  relates to static pressure  
 $t$  tip  
 $z$  axial direction  
 $\theta$  tangential direction  
 $1$  measuring station at rotor inlet  
 $2$  measuring station at rotor exit

Superscripts:

$\bar{\phantom{x}}$  indicates an average value  
 $'$  relative to rotor

## APPENDIX B

## EQUATIONS

## Blade-Element Calculations

Net positive suction head:

$$H_{SV} = H_1 - h_v \quad (B1)$$

Ideal head rise:

$$\begin{aligned} \Delta H_i &= \frac{U_2 V_{\theta,2} - U_1 V_{\theta,1}}{g} \\ &= \frac{U_2 V_{\theta,2}}{g} \quad (\text{assuming } V_{\theta,1} = 0) \end{aligned} \quad (B2)$$

Head rise coefficient:

$$\psi = \frac{\Delta H}{U_t^2/g} \quad (B3)$$

Ideal head rise coefficient:

$$\psi_i = \frac{\Delta H_i}{U_t^2/g}$$

Flow coefficient:

$$\phi = \frac{V_z}{U_t} \quad (B4)$$

Relative total-pressure loss coefficient:

$$\begin{aligned} \bar{\omega} &= \frac{H'_{2,i} - H'_2}{V_1'^2/2g} \\ &= \frac{\Delta H_i - \Delta H}{V_1'^2/2g} \end{aligned} \quad (B5)$$

Incidence angle:

$$i = \beta_1' - \gamma_1 \quad (B6)$$

Deviation angle:

$$\delta = \beta_2' - \gamma_2 \quad (B7)$$

Efficiency:

$$\eta = \frac{\Delta H}{\Delta H_1} \quad (B8)$$

Cavitation number:

$$k = \frac{h_1 - h_v}{V_1'^2 / 2g} \quad (B9)$$

#### Overall Performance Calculations

Average flow coefficient:

$$\varphi = \frac{\bar{V}_{z,1}}{U_t} \quad (B10)$$

Average inlet axial velocity:

$$\bar{V}_{z,1} = \frac{Q_m}{448.8 \pi (r_t^2 - r_h^2)} \quad (B11)$$

Mass-averaged inlet total head:

$$\bar{H}_1 = \frac{\int_{r_h}^{r_t} V_{z,1} r_1 H_1 dr_1}{\int_{r_h}^{r_t} V_{z,1} r_1 dr_1} \quad (B12)$$

Mass-averaged outlet total head:

$$\bar{H}_2 = \frac{\int_{r_h}^{r_t} V_{z,2} r_2 H_2 dr_2}{\int_{r_h}^{r_t} V_{z,2} r_2 dr_2} \quad (B13)$$

Mass-averaged head rise coefficient:

$$\bar{\psi} = \frac{g}{U_t^2} (\bar{H}_2 - \bar{H}_1) \quad (B14)$$

Mass-averaged efficiency:

$$\bar{\eta} = \frac{\int_{r_h}^{r_t} V_{z,2} r_2 \eta dr_2}{\int_{r_h}^{r_t} V_{z,2} r_2 dr_2} \quad (B15)$$

$H_{SV}$  normalized to  $N = 9000$  rpm:

$$(H_{SV})_N = H_{SV} \left( \frac{9000}{N} \right)^2 \quad (B16)$$

## APPENDIX C

## EFFECT OF MASS-FLOW REDISTRIBUTIONS OF DEVIATION ANGLE

For simplicity, the calculation of deviation angle, defined as

$$\delta = \beta_2' - \gamma_2 \quad (B7)$$

assumes that the flow across the blade row under all flow conditions occurs along cylindrical surfaces; that is, the velocity diagram computed at the measuring station occurs at the same radius at the blade trailing edge. For investigations where the blade exit measurements are taken relatively close to the rotor trailing edge or the recorded mass-flow shifts are small, this assumption does not affect the calculation significantly. Since both of these conditions were violated during certain modes of operation reported herein, an effort was made to transfer the velocity diagrams computed at the measuring station (located approximately 1 in. downstream of the rotor trailing edge) to the point where the streamline leaves the blade trailing edge. The problem which arises is that, although the intersection of the streamline and measuring station (equal percentage of weight flow carried from tip to streamline radius) could be computed, the streamline curvature through the blade remains unknown. Accordingly, the following procedure was used:

(1) Several radii (less than the outlet measuring station radius) are selected at which the streamline is assumed to leave the blade trailing edge.

(2) Axial and absolute tangential velocities occurring at the blade trailing-edge station are computed from

$$V_{z,te} = \frac{r_t^2 - r_{ms}^2}{r_t^2 - r_{te}^2} V_{z,ms}$$

$$V_{\theta,te} = \frac{r_{ms}}{r_{te}} V_{\theta,ms}$$

where ms and te signify values at the instrument measuring station and blade trailing edge, respectively.

(3) Velocity diagrams and deviation angles are computed with blade speed and blade angle at each assumed radial location  $r_{te}$ .

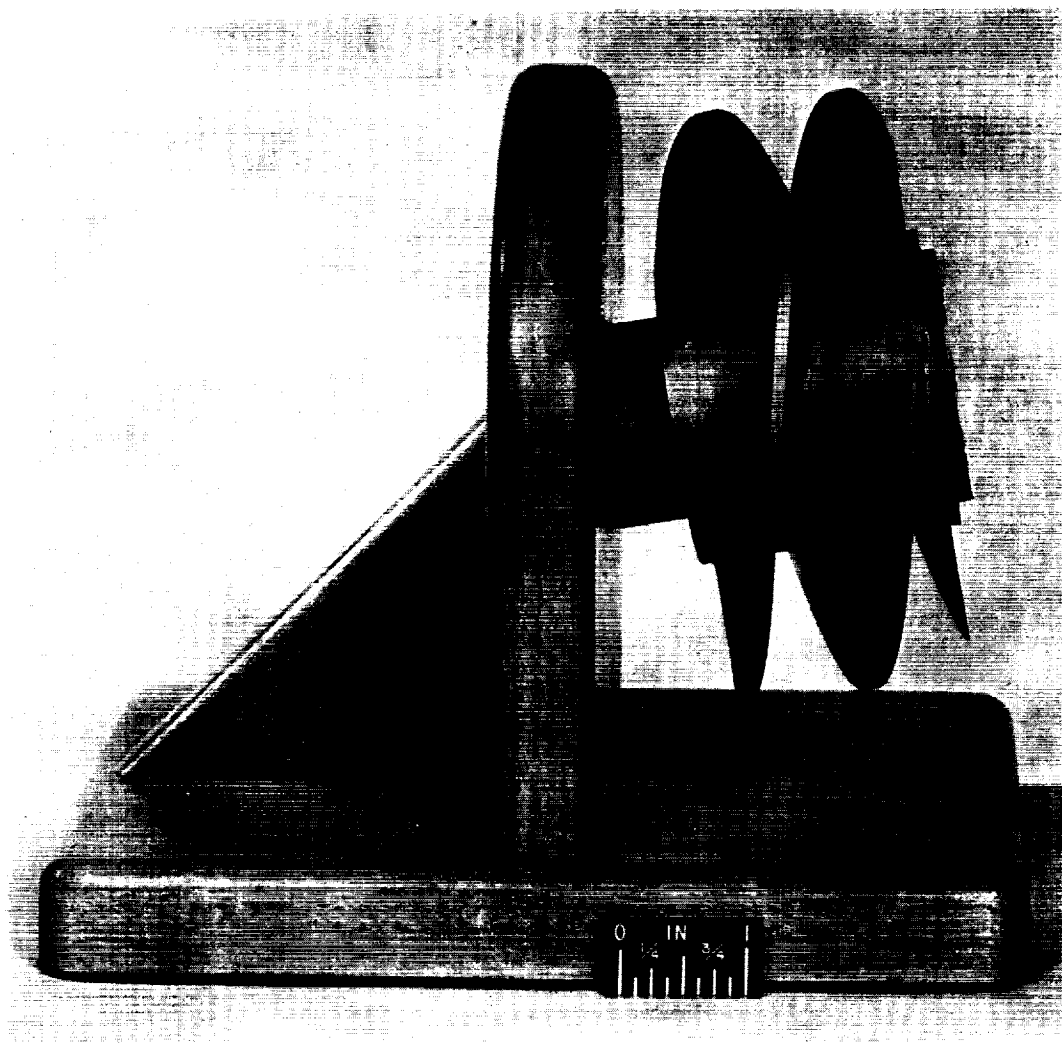
Calculations based on this procedure and applied to the measurements taken at  $r = 2.365$  showed that, if the streamline is assumed to leave the blade trailing edge at a radius of from 0.050 to 0.070 inch less than the measuring station radius, positive deviation angles were computed.

#### REFERENCES

1. Ross, C. C., and Banerian, Gordon: Some Aspects of High-Suction Specific-Speed Pump Inducers. Trans. ASME, vol. 78, no. 8, Nov. 1956, pp. 1715-1721.
2. Acosta, A. J.: An Experimental Study of Cavitating Inducers. Paper presented at Second Symposium on Naval Hydrodynamics (Wash., D.C.), Aug. 25, 1958.
3. Crouse, James E., Montgomery, John C., and Soltis, Richard F.: Investigation of the Performance of an Axial-Flow-Pump Stage Designed by the Blade-Element Theory - Design and Overall Performance. NASA TN D-591, 1961.
4. Montgomery, John C.: Analytical Performance Characteristics and Outlet Flow Conditions of Constant and Variable Lead Helical Inducers for Cryogenic Pumps. NASA TN D-583, 1961.
5. Rains, Dean A.: Tip Clearance Flows in Axial Flow Compressors and Pumps. Rep. 5, Hydrodynamics and Mech. Eng. Labs., C.I.T., June 1954.
6. Huppert, M. C., King, W. S., and Stripling, L. B.: Some Cavitation Problems in Rocket Propellant Pumps. Rocketdyne, Div. North Am. Aviation, Inc., 1960.
7. Spannhake, Wilhelm: Centrifugal Pumps, Turbines, and Propellers. The Technology Press, M.I.T., 1934.
8. Stepanoff, Alexey Joakim: Centrifugal and Axial-Flow Pumps. Second ed., John Wiley & Sons, Inc., 1957.
9. Wu, Chung-Hua: A General Theory of Three-Dimensional Flow in Subsonic and Supersonic Turbomachines of Axial-, Radial-, and Mixed-Flow Types. NACA TN 2604, 1952.
10. Stripling, L. B.: Cavity Flow in Cascades. Rocketdyne, Div. North Am. Aviation, Inc., 1960.

TABLE I. - BLADE GEOMETRY OF 78° HELICAL INDUCER

Rotor tip diameter, in.	4.956	}	Constant
Rotor hub diameter, in.	2.478		
Hub-tip ratio	0.5		
Radial tip clearance, in.	0.030		
Tip clearance ratio	0.0242		$\frac{\text{Tip clearance}}{\text{Blade height}}$
Number of blades	3		
Chord length at tip, in.	9.620		
Chord length at hub, in.	5.120		
Solidity at tip	1.856		
Solidity at hub	1.973		
Blade thickness at tip, in.	0.10	}	Linear variation
Blade thickness at hub, in.	0.19		

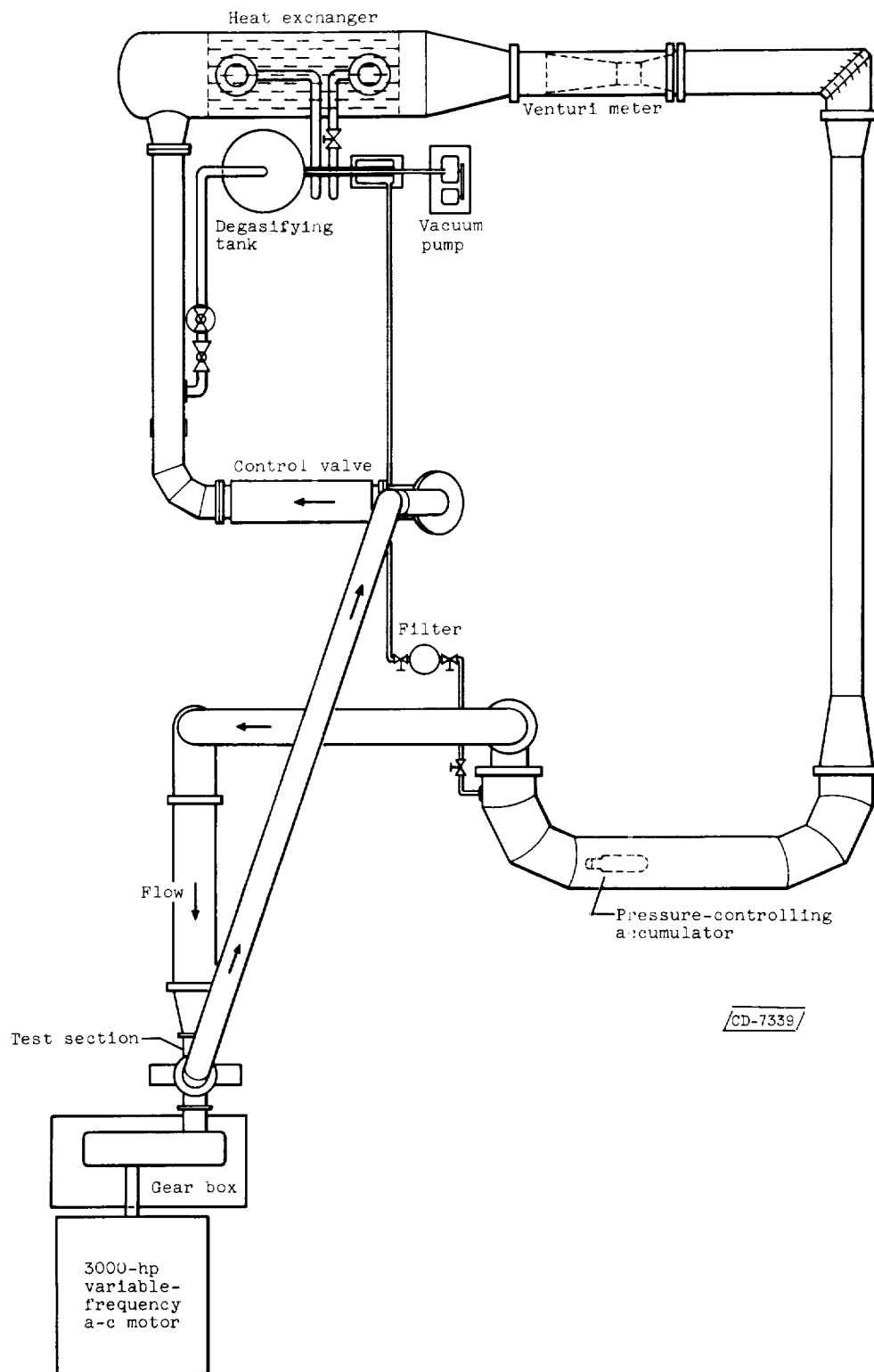


C-49047

Figure 1. -  $78^{\circ}$  Helical inducer.

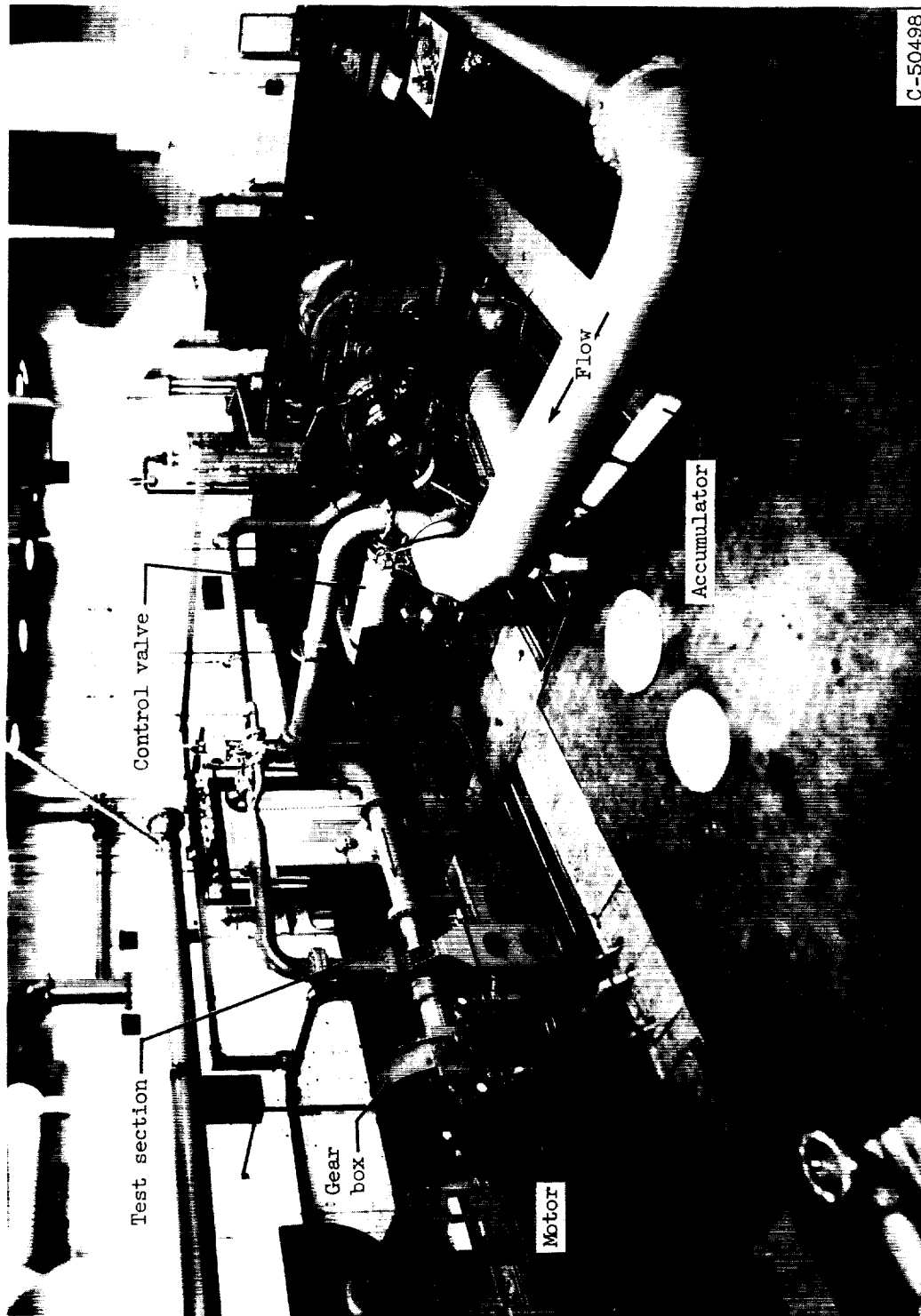


E-1368



(a) Schematic diagram.

Figure 2. - Test facility.



(b) Photograph.

Figure 2. - Concluded. Test facility.

E-1368

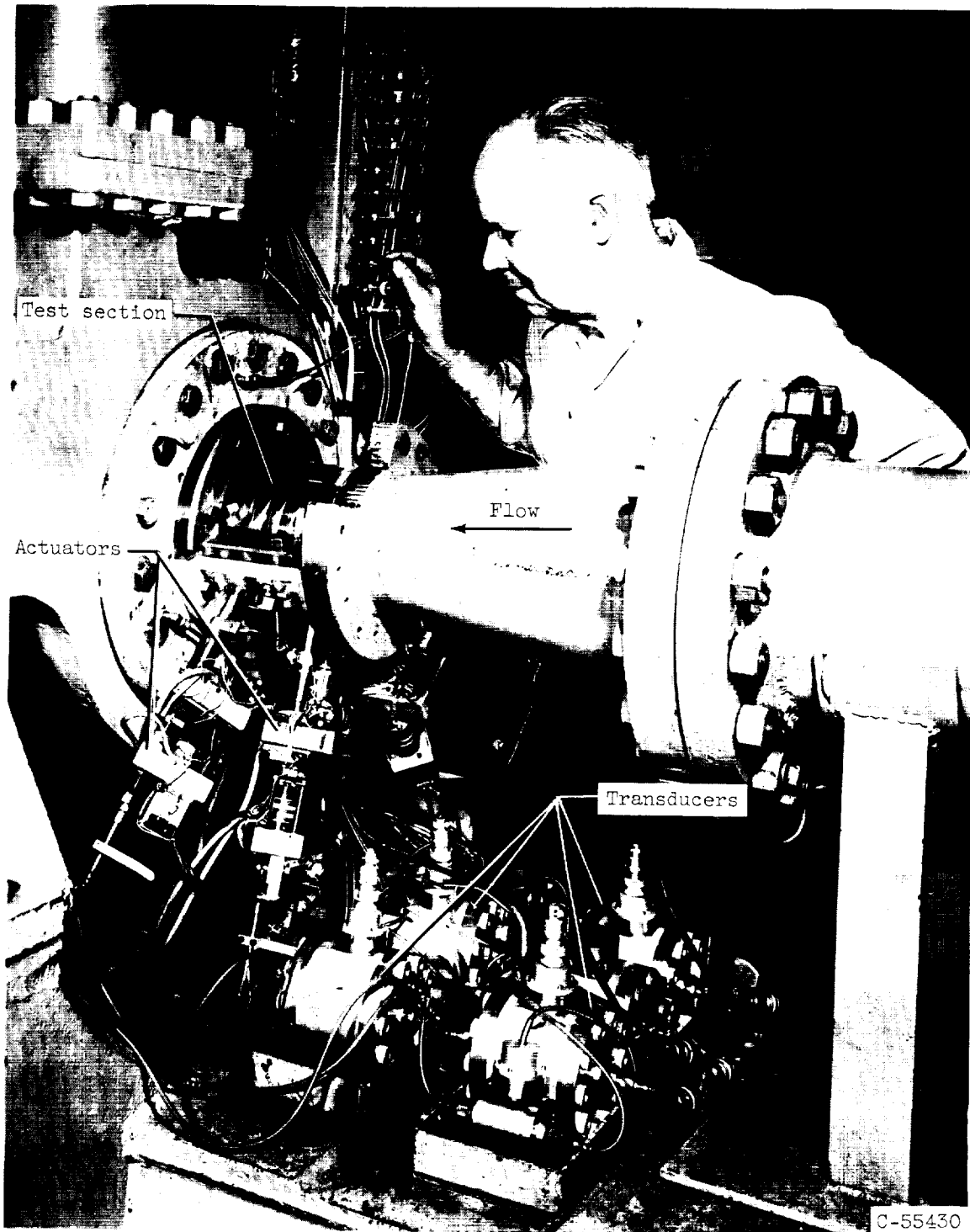


Figure 3. - Test section showing rotor installed and location of instrumentation.

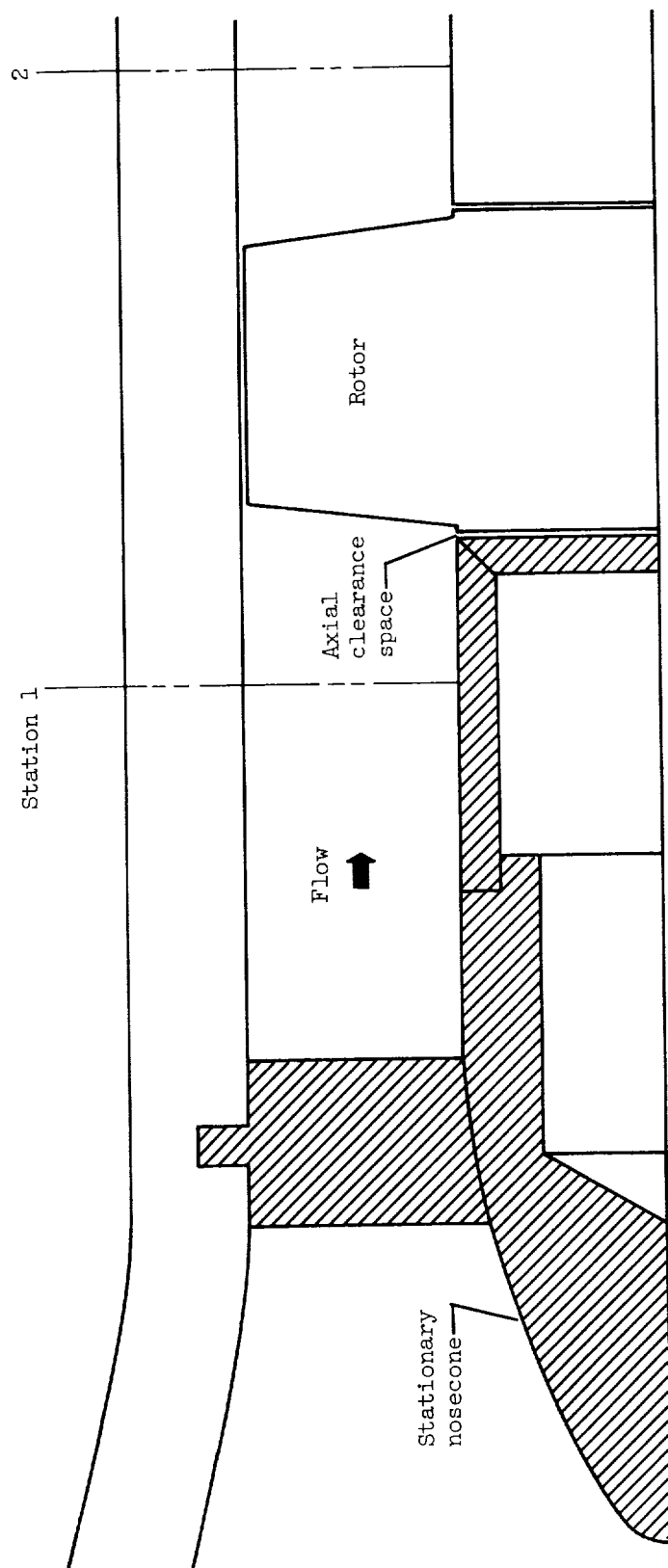


Figure 4. - Test section.

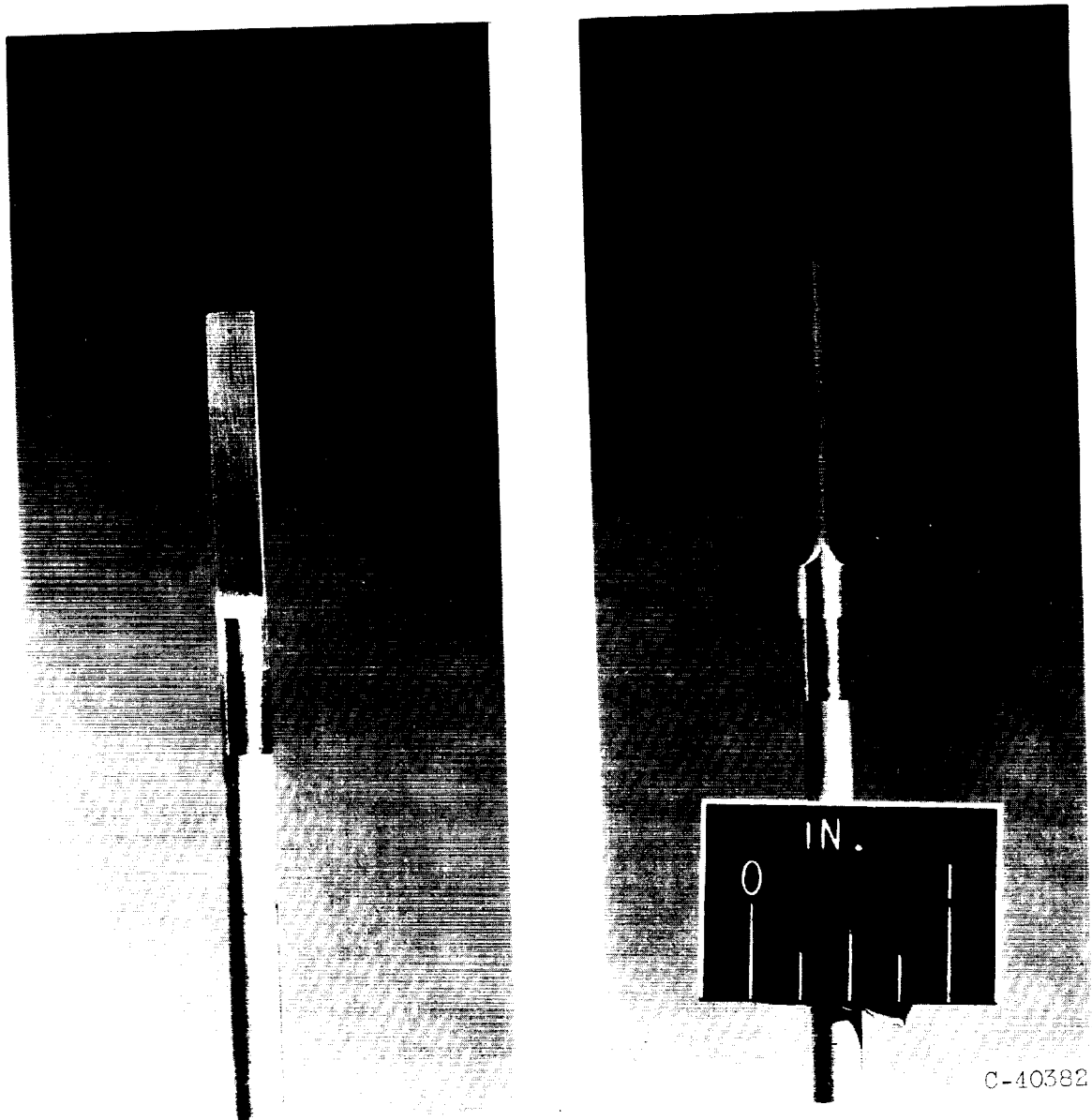
R9CT-ET



C-55432

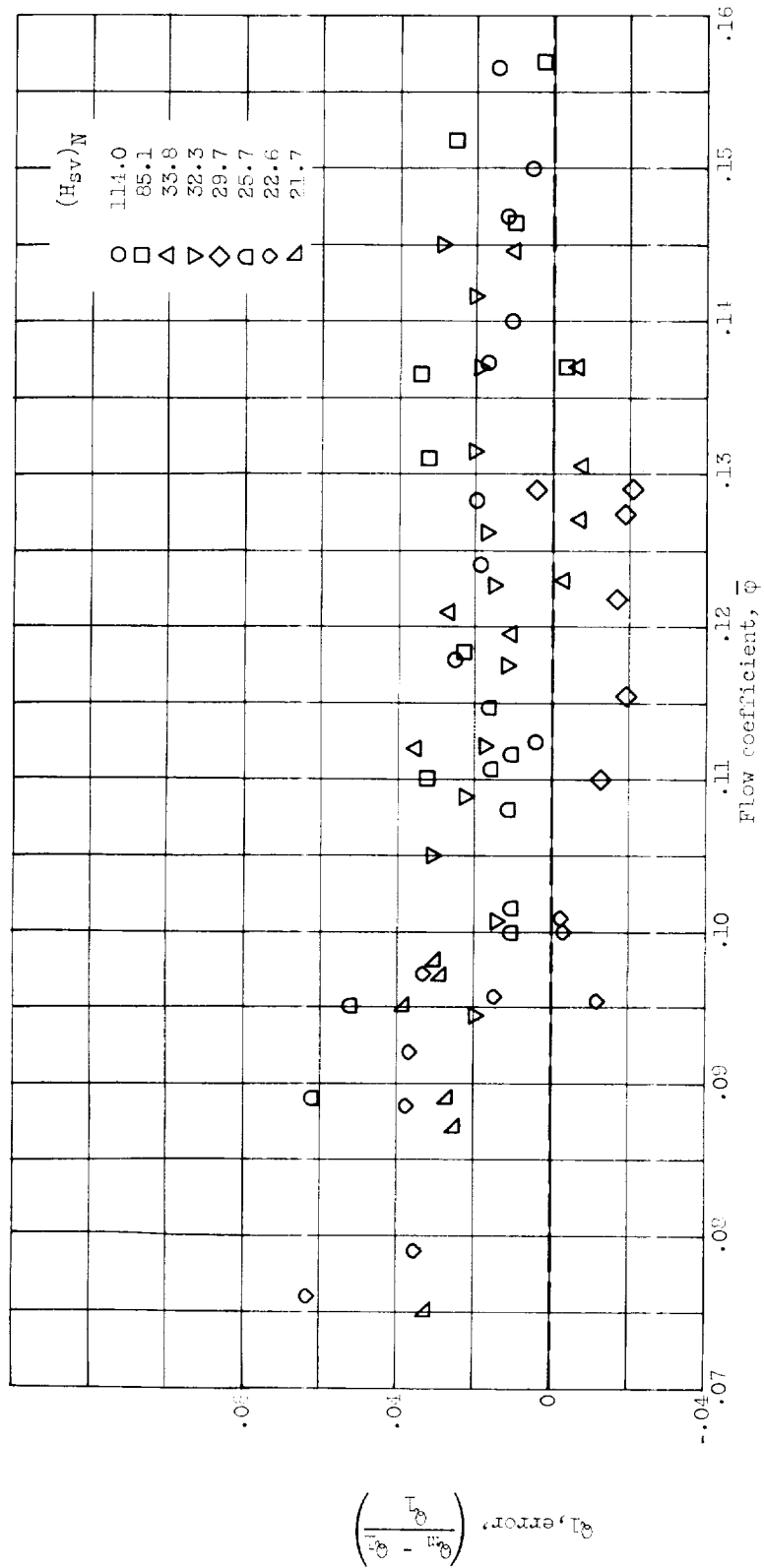
(a) Total-pressure claw.

Figure 5. - Probes.



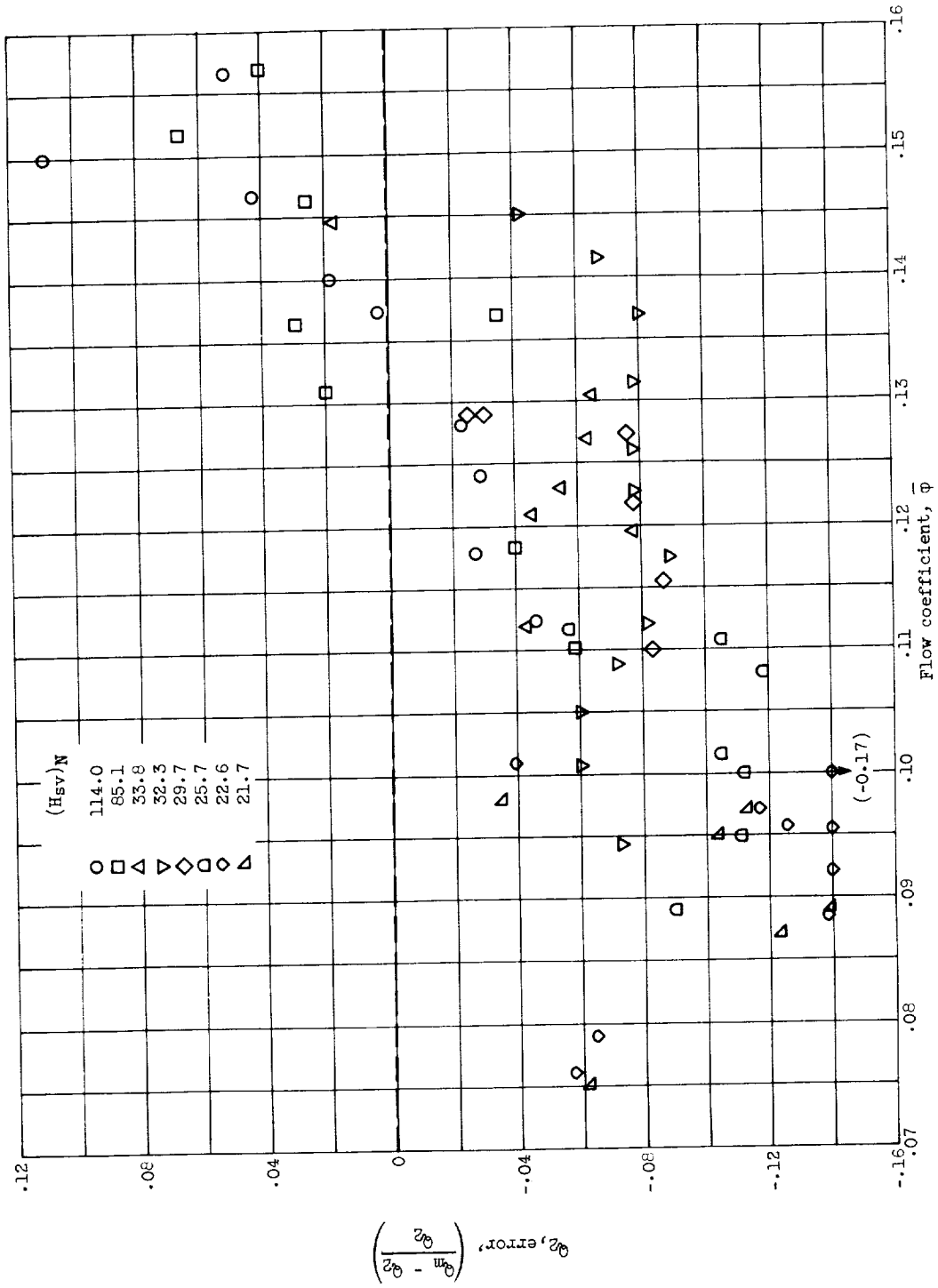
(b) Static-pressure wedge.

Figure 5. - Concluded. Probes.



(a) Inducer inlet flow.

Figure 6. - Comparison of integrated flow with flow measured by Venturi meter.



(b) Inducer outlet flow.

Figure 6. - Concluded. Comparison of integrated flow with flow measured by Venturi meter.



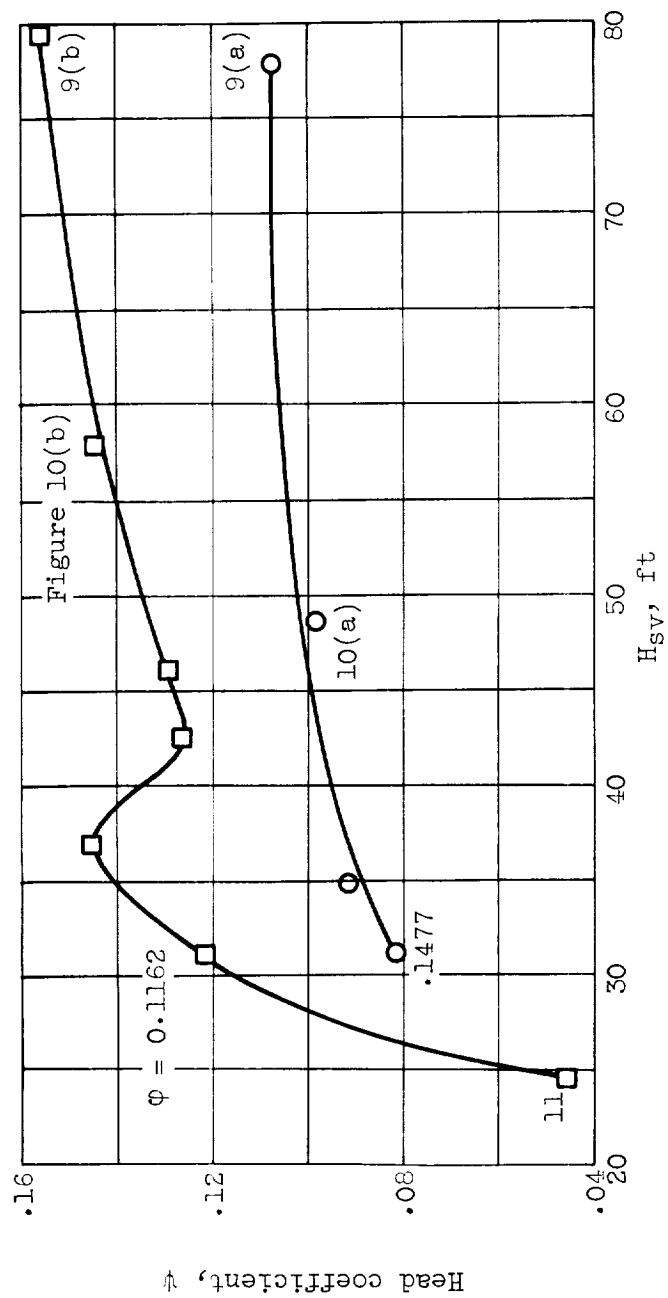
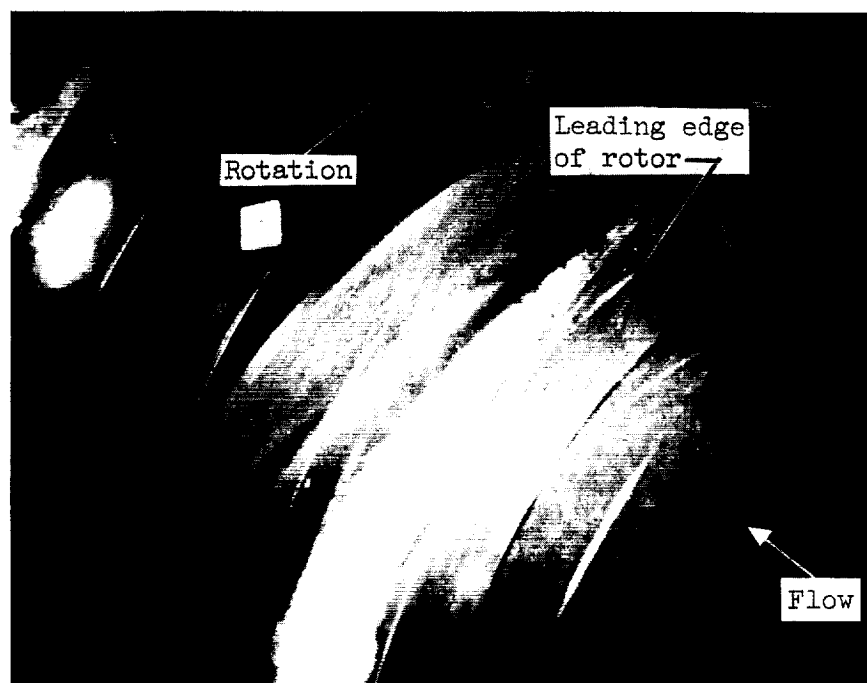


Figure 7. - Performance curve with location of photographs.



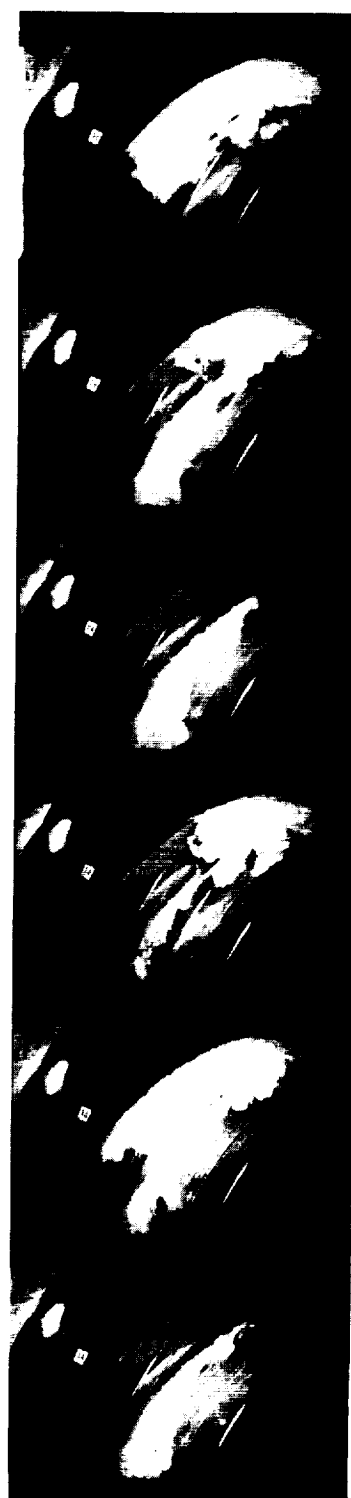
(a)  $\phi = 0.1477$ .



(b)  $\phi = 0.1162$ .

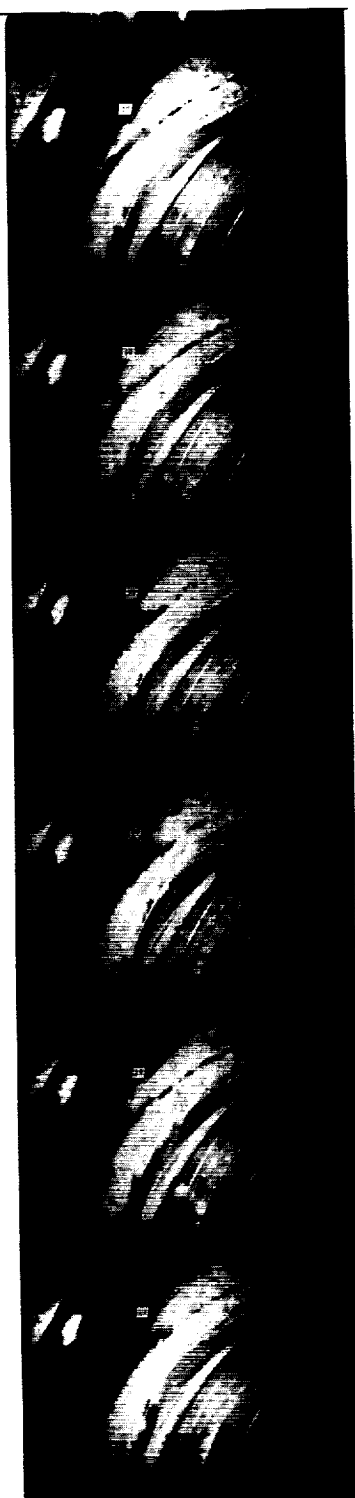
C-58105

Figure 8. - Tip vortex cavitation illustrated at high  $H_{sv}$ .

(a)  $\phi = 0.1477$ .(b)  $\phi = 0.1162$ .

C-58106

Figure 9. - Sequence showing unsteady type of cavitation.



C-58107

Figure 10. - Steady-type cavitation in "breakdown region."  $\phi = 0.1162$ .

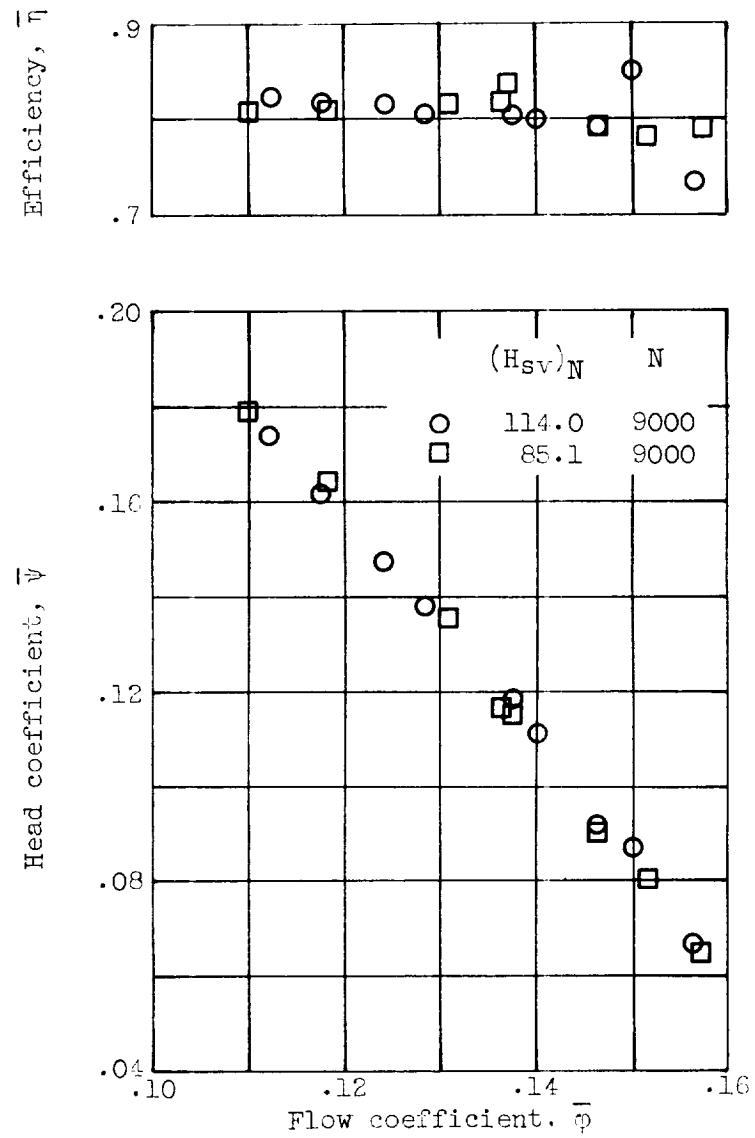


Figure 11. - Overall performance at noncavitating conditions.

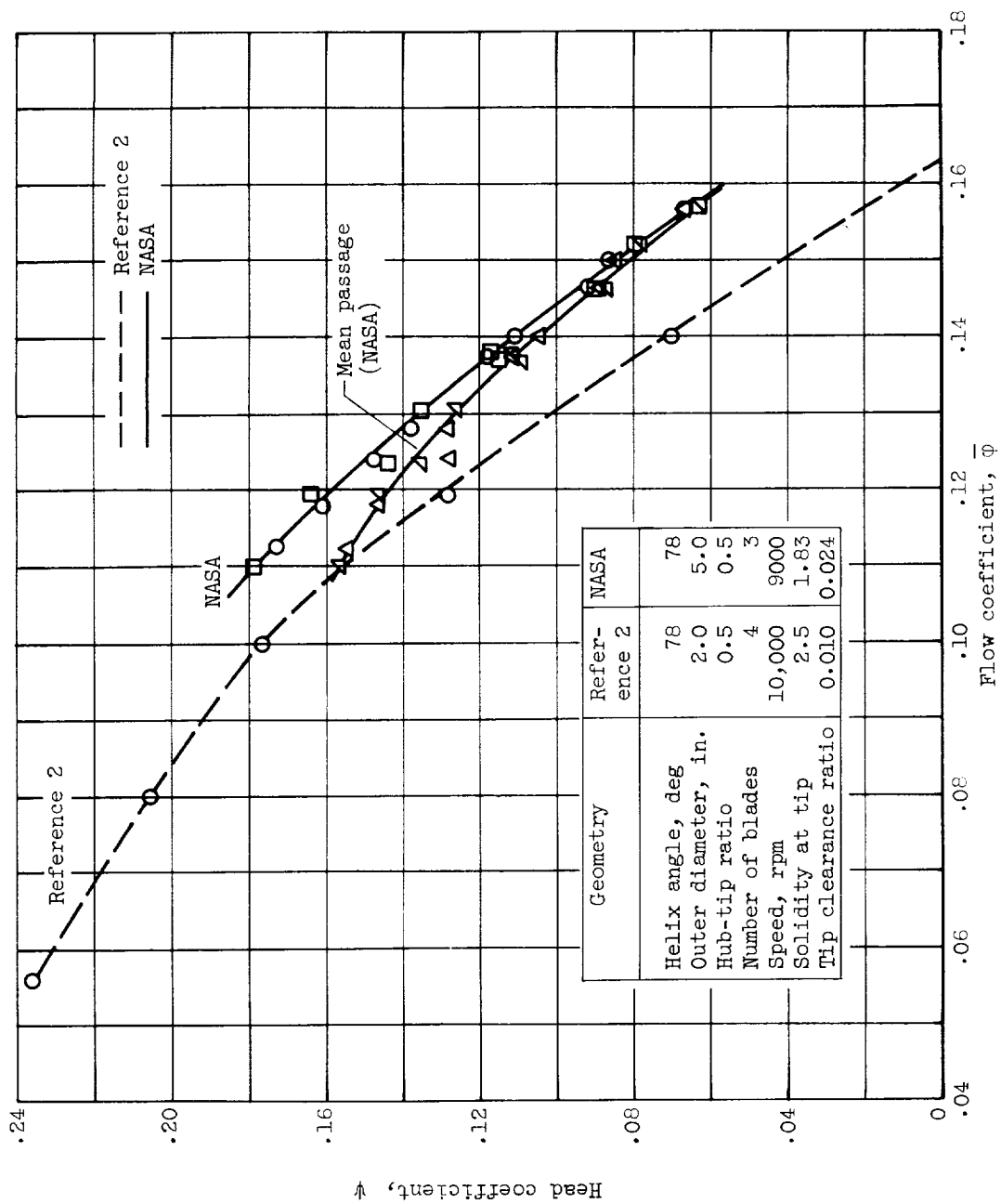


Figure 12. - Comparison of overall noncavitating performance with results reported in reference 2.

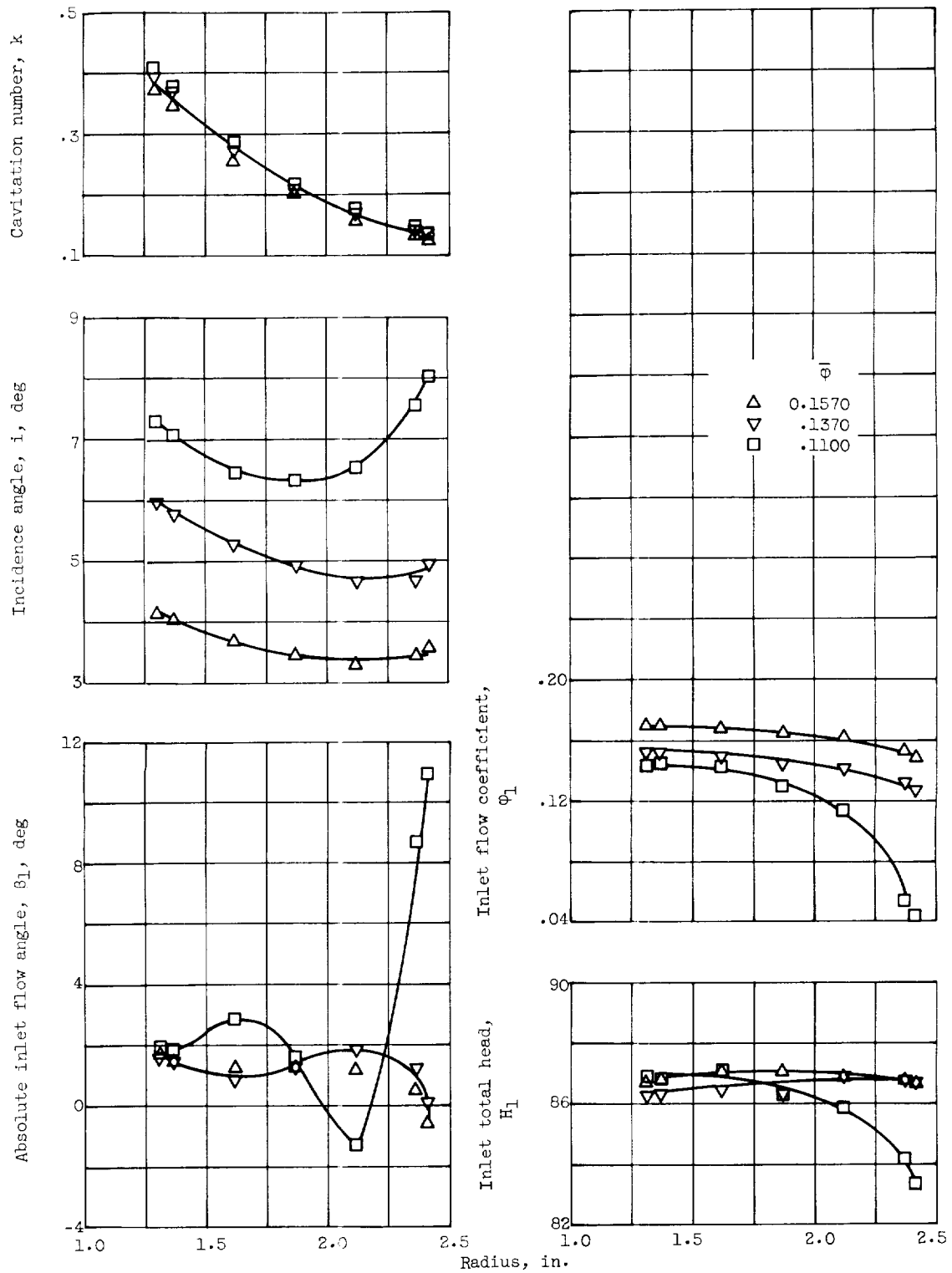


Figure 13. - Radial distribution of flow conditions and blade-element performance parameters (inlet noncavitating conditions). ( $H_{sv}$ )<sub>N</sub>, 85.1 feet.

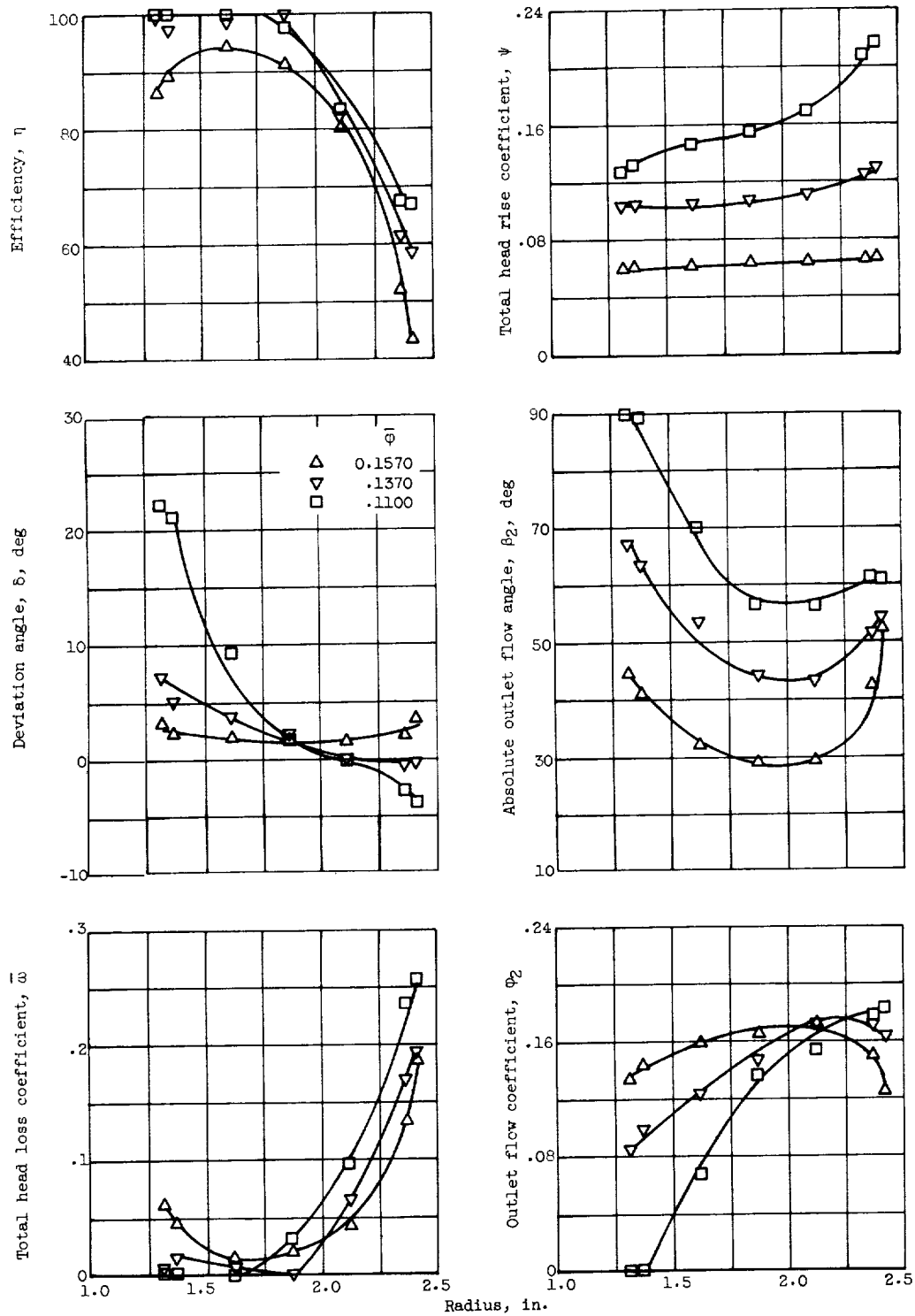


Figure 14. - Radial distribution of outlet parameters for noncavitating conditions.  $(H_{sv})_N$ , 85.1 feet.



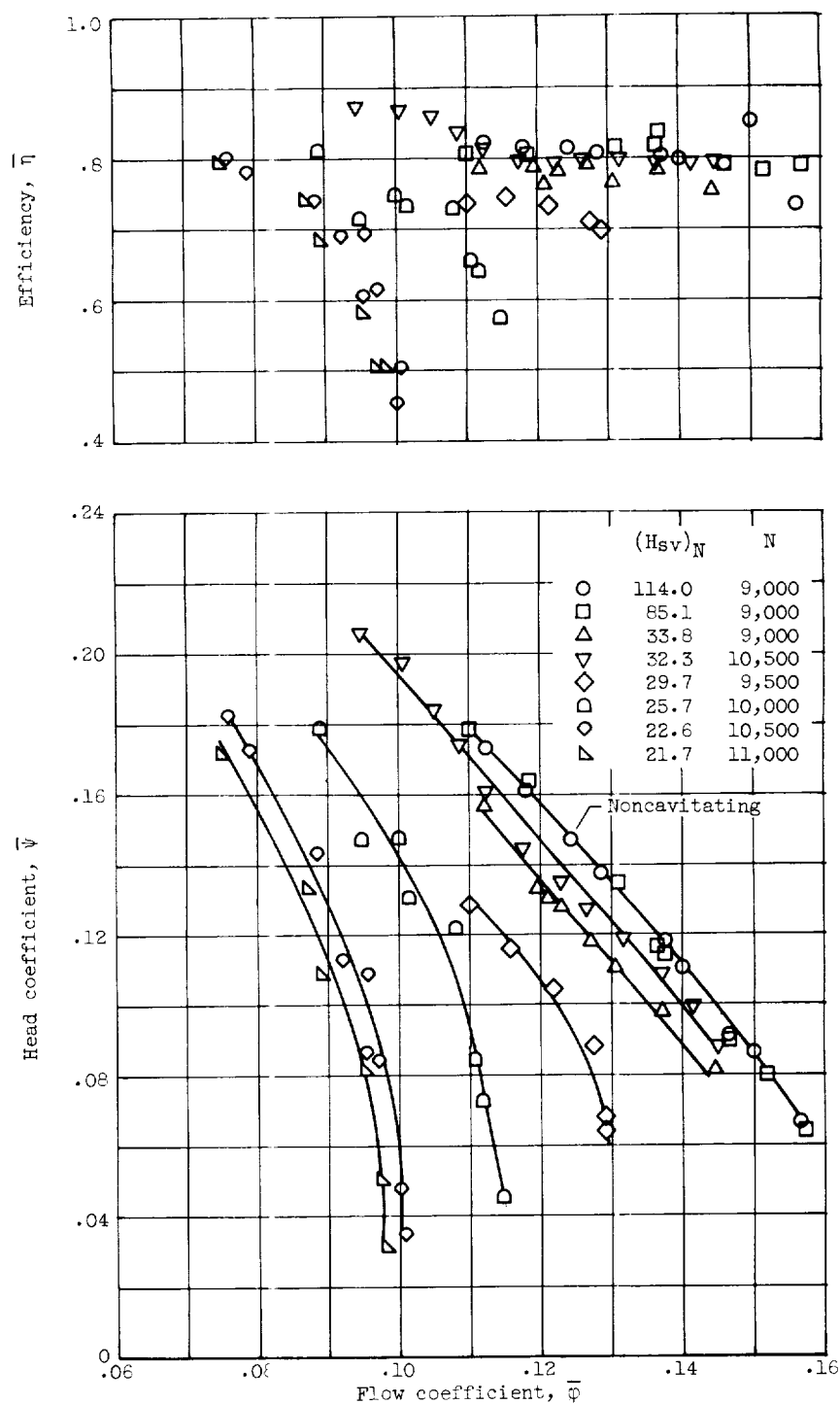


Figure 15. - Overall performance (cavitating and noncavitating conditions).

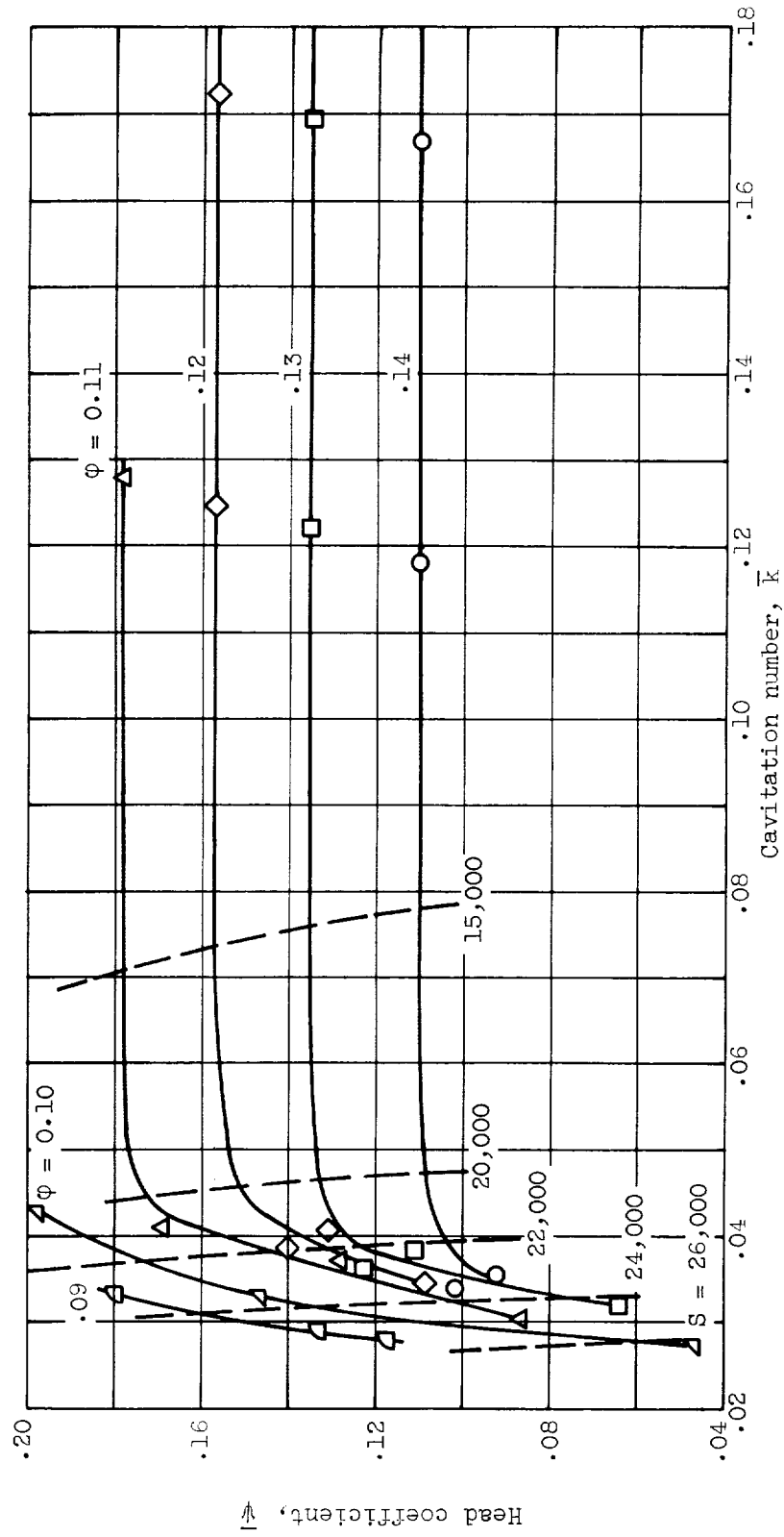


Figure 16. - Inducer performance as a function of  $\bar{k}$ .

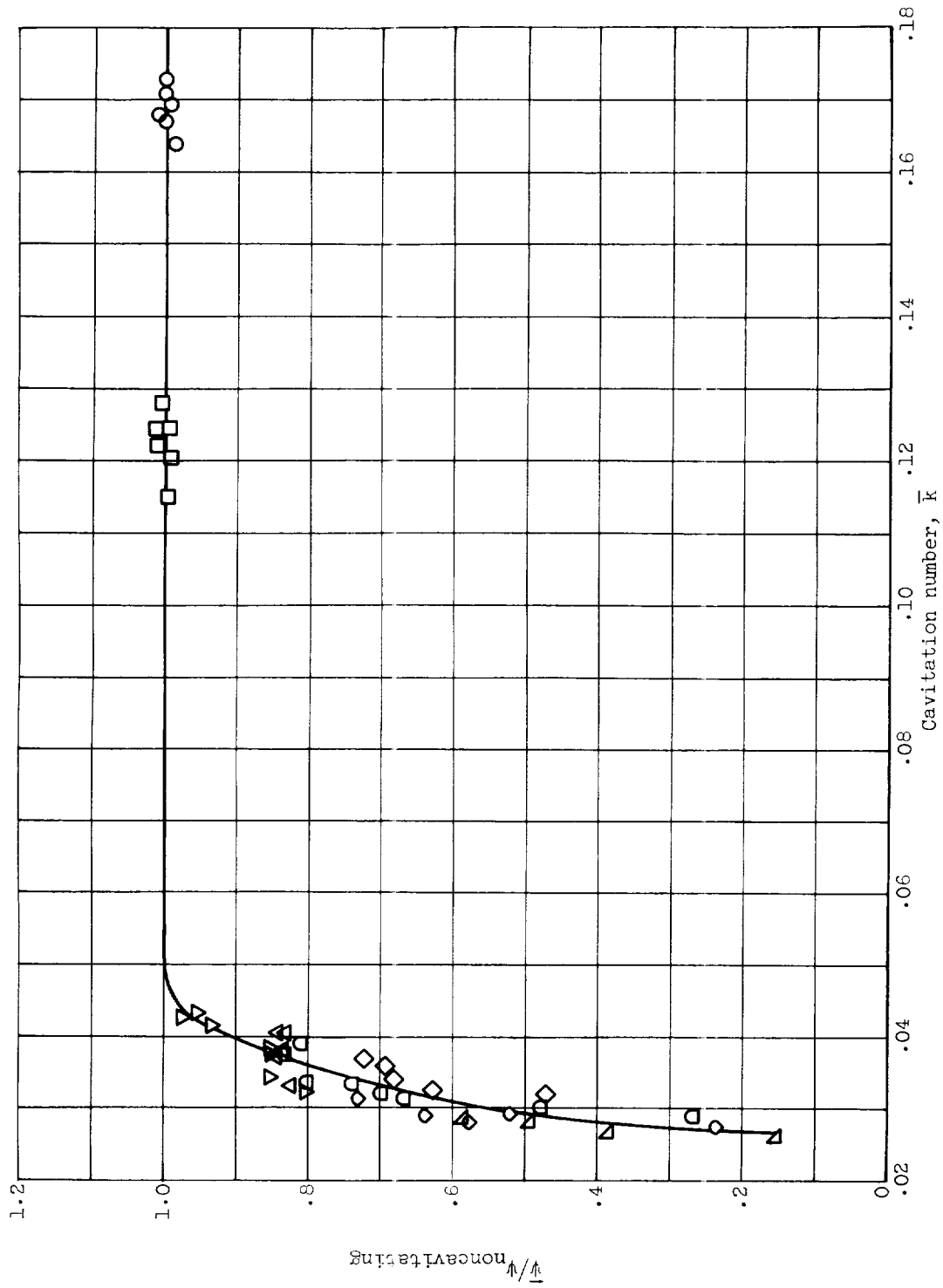


Figure 17. - Composite of cavitation performance.

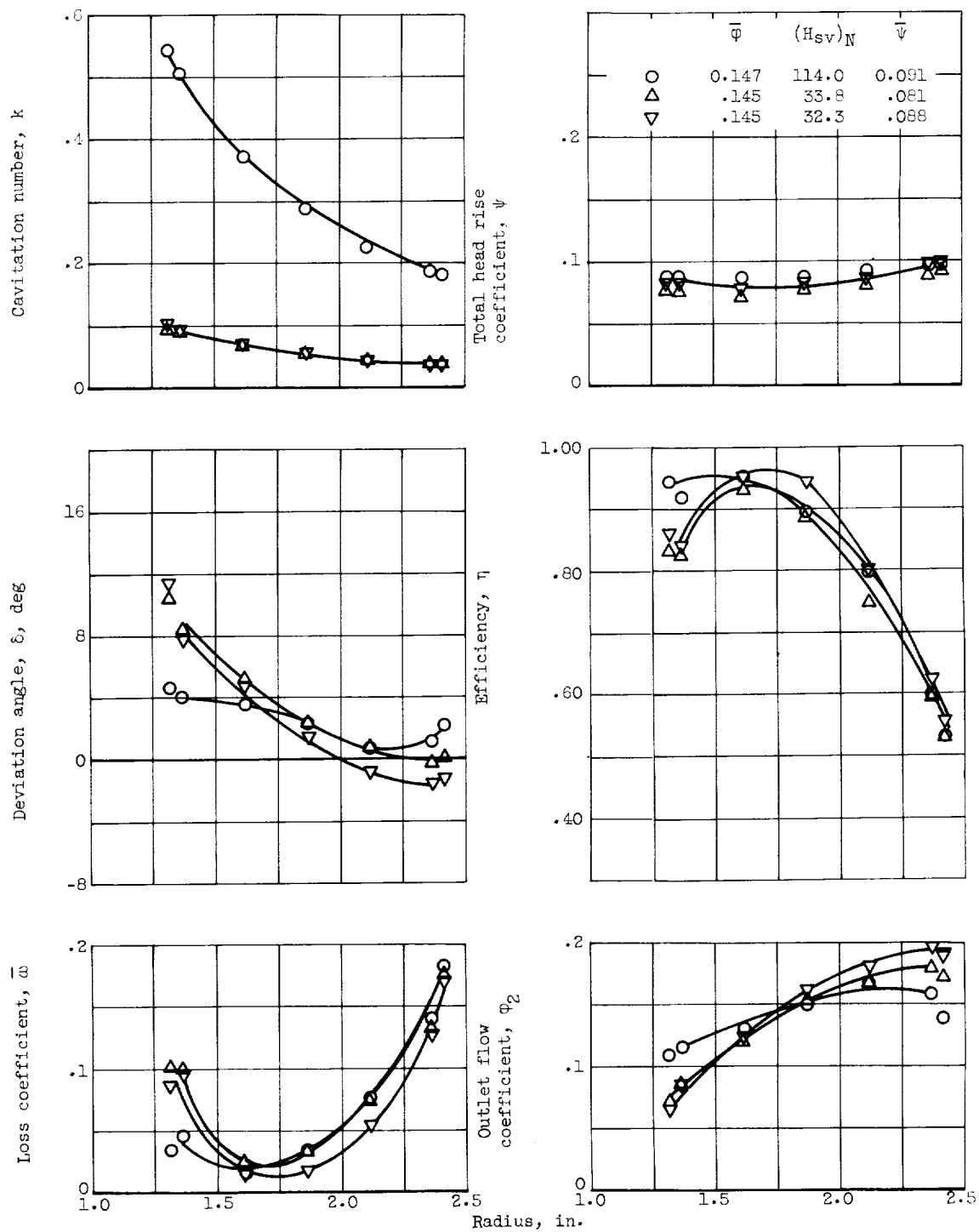
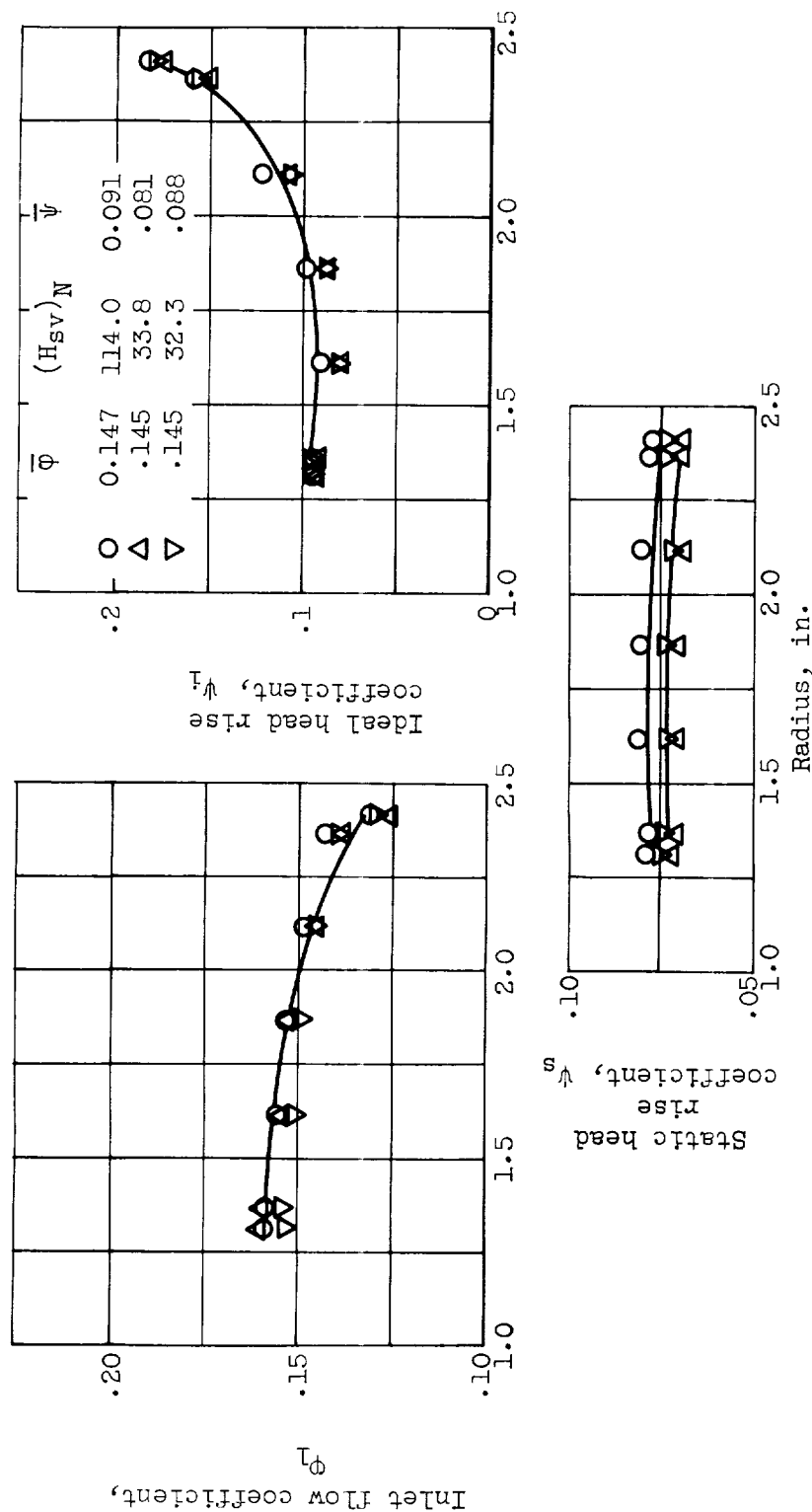
(a)  $\phi \approx 0.145$ .

Figure 18. - Radial distribution of flow conditions and blade-element performance parameters (cavitating and noncavitating conditions).



(a) Concluded.  $\phi \approx 0.145$ .

Figure 18. - Continued. Radial distribution of flow conditions and blade-element performance parameters (cavitating and noncavitating conditions).

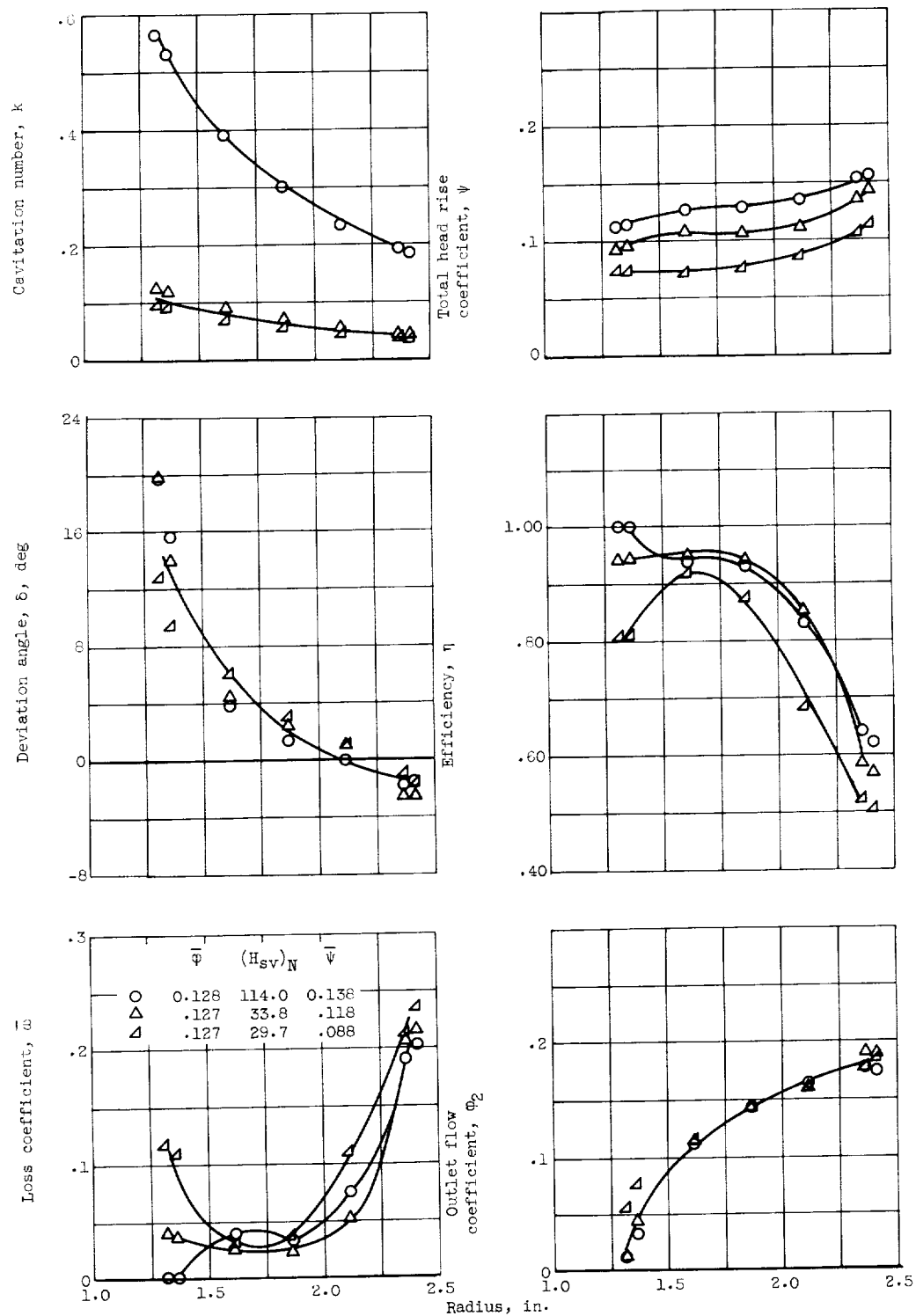
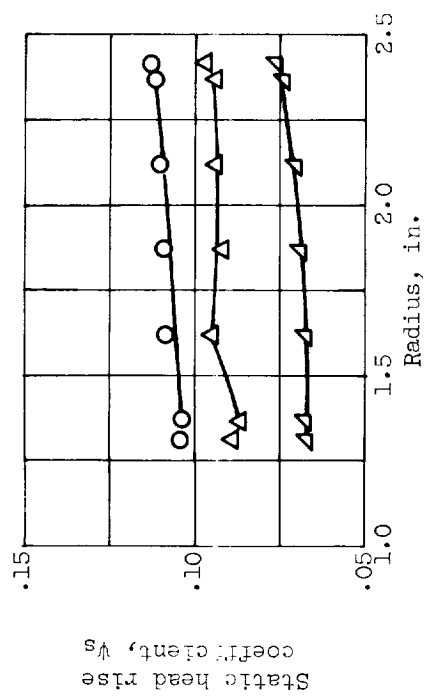
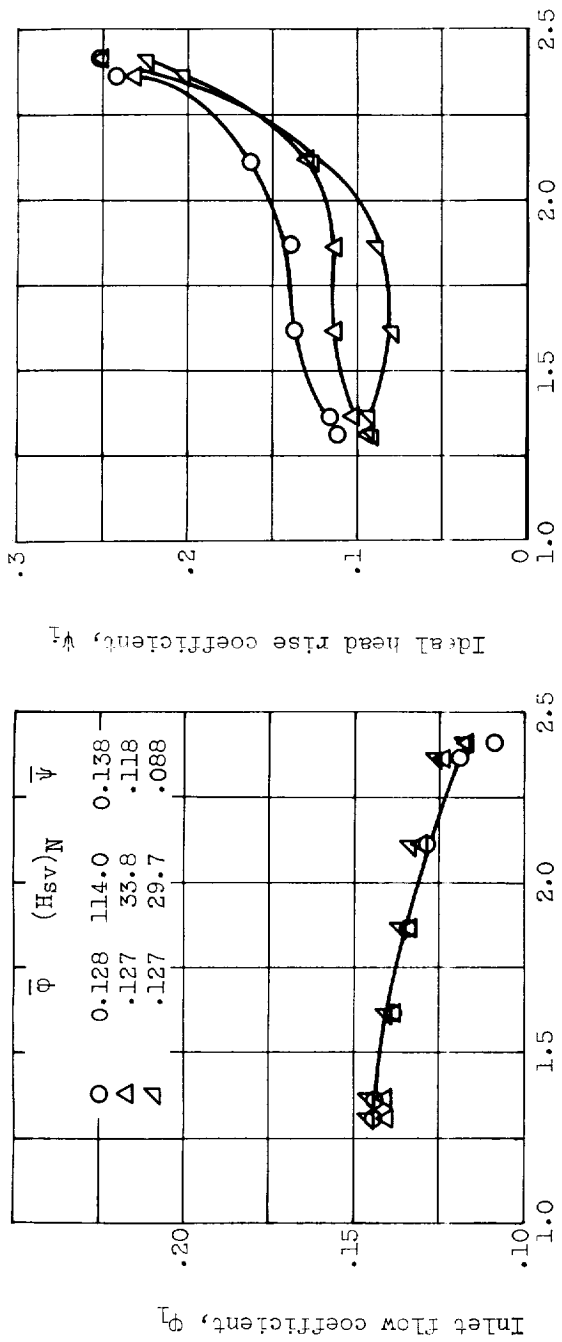
(b)  $\phi \approx 0.128$ .

Figure 18. - Continued. Radial distribution of flow conditions and blade-element performance parameters (cavitating and noncavitating conditions).



(b) Concluded.  $\phi \approx 0.128$ .

Figure 18. - Continued. Radial distribution of flow conditions and blade-element performance parameters (cavitating and noncavitating conditions).

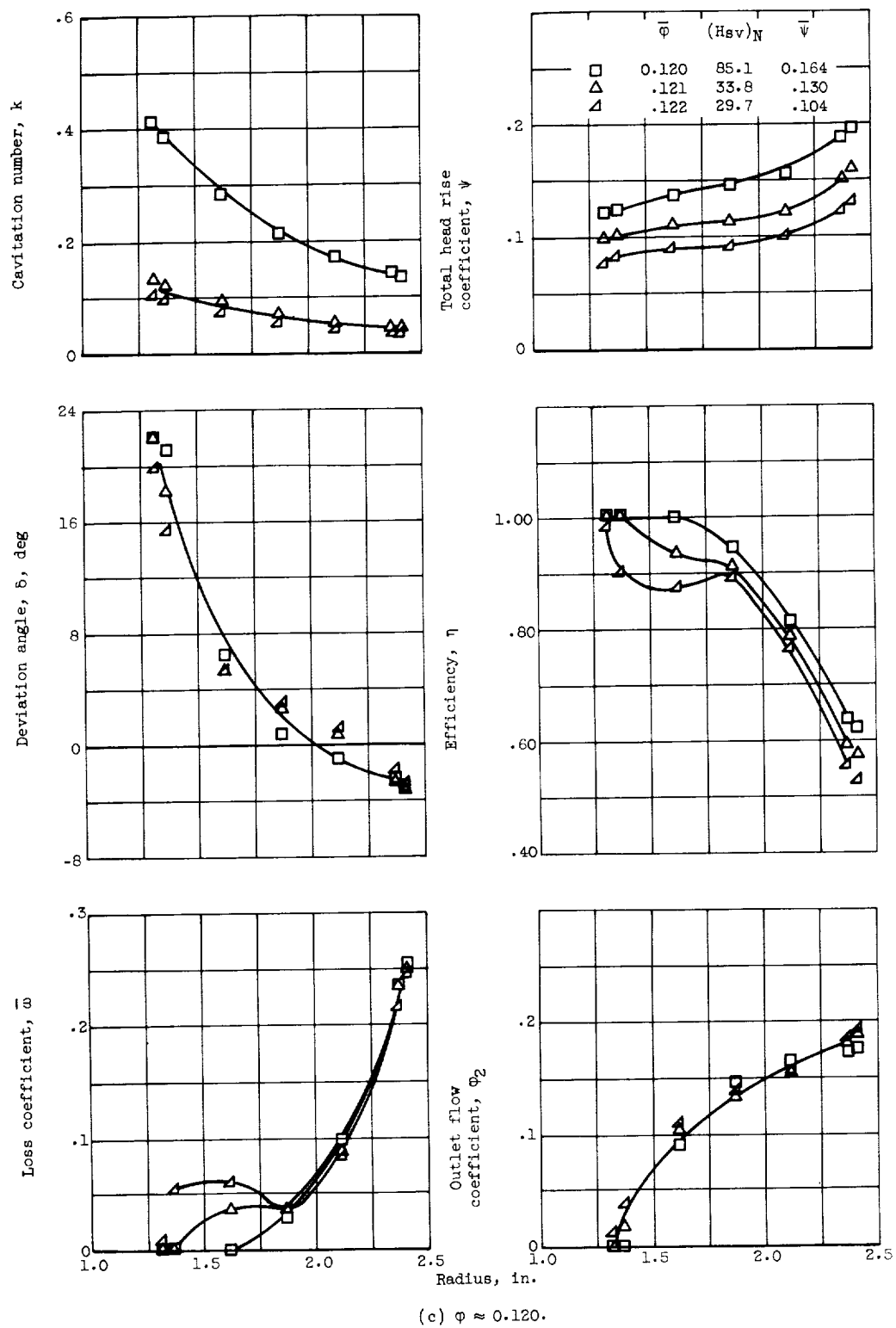


Figure 18. - Continued. Radial distribution of flow conditions and blade-element performance parameters (cavitating and noncavitating conditions).



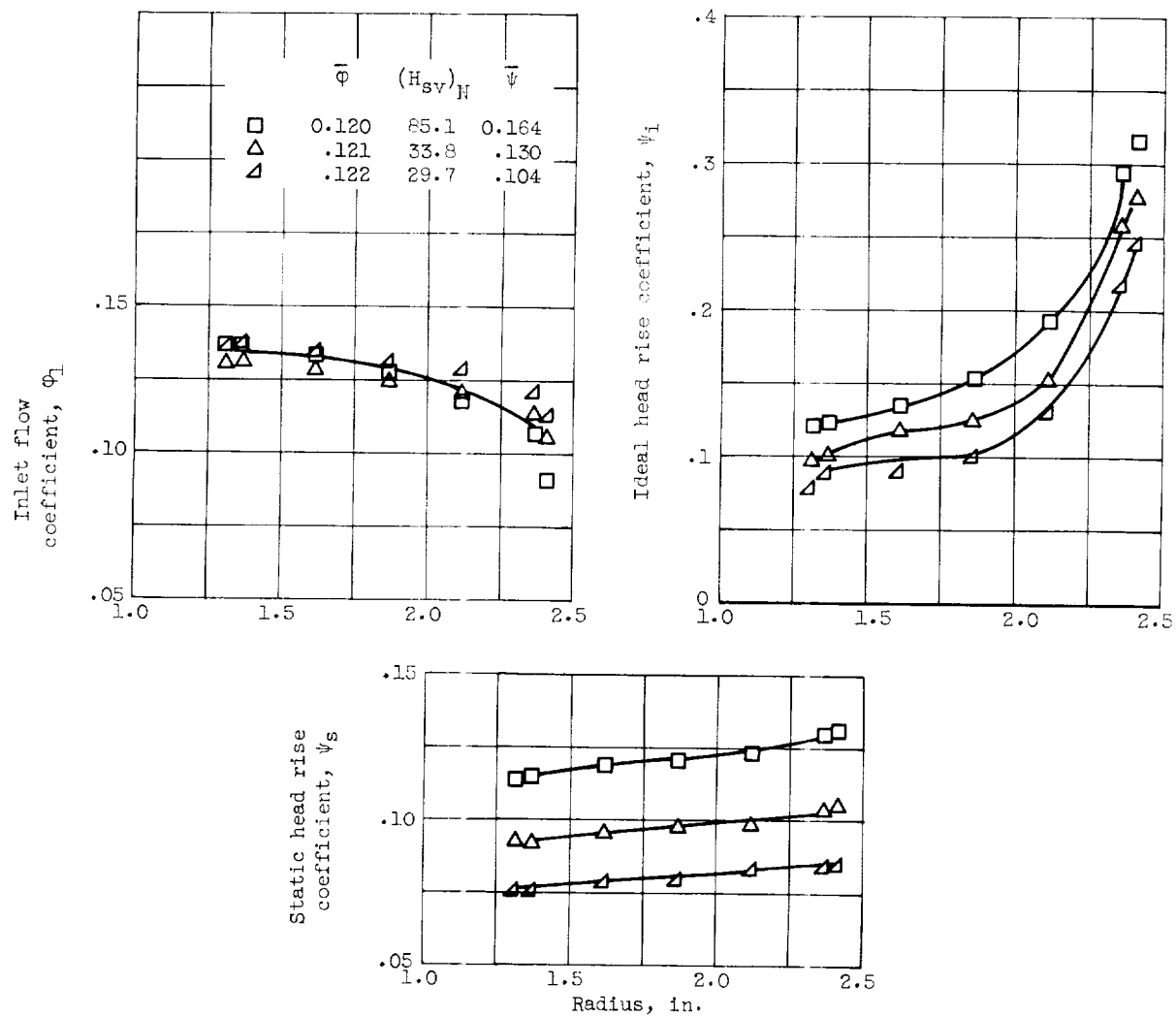
(c) Concluded.  $\phi \approx 0.120$ .

Figure 18. - Continued. Radial distribution of flow conditions and blade-element performance parameters (cavitating and noncavitating conditions).

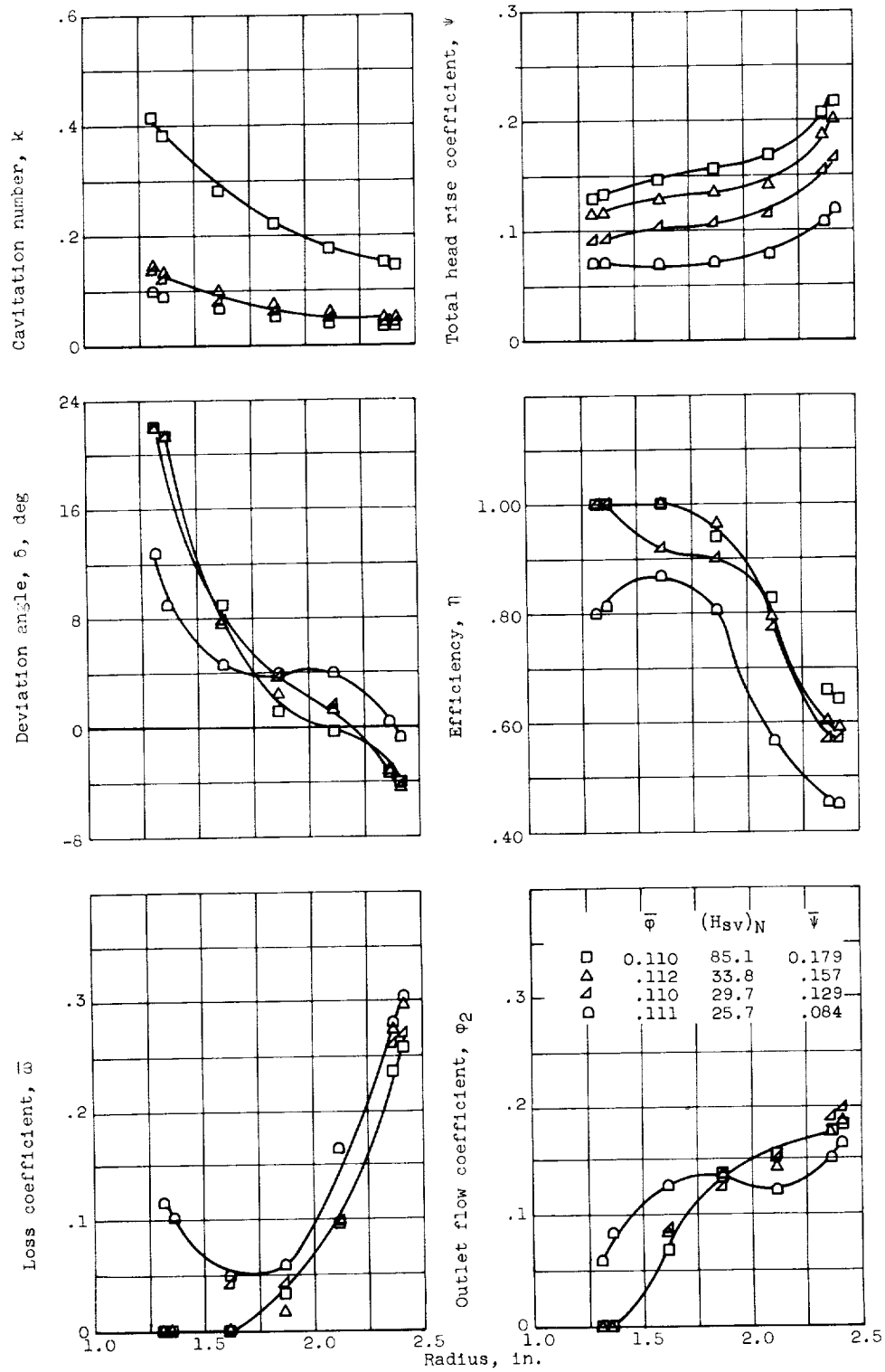
(d)  $\phi \approx 0.110$ .

Figure 18. - Continued. Radial distribution of flow conditions and blade-element performance parameters (cavitating and noncavitating conditions).

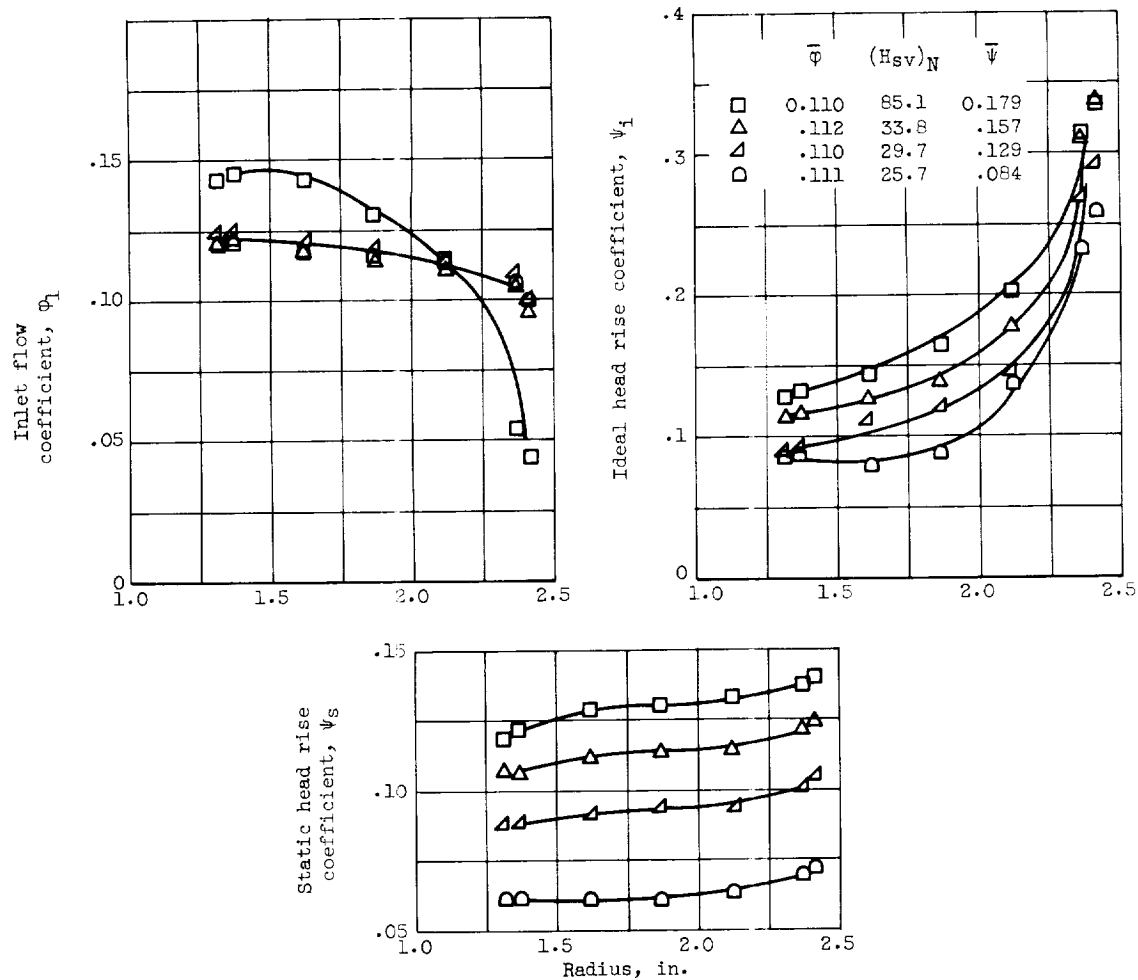
(d) Concluded.  $\phi \approx 0.110$ .

Figure 1E. - Continued. Radial distribution of flow conditions and blade-element performance parameters (cavitating and noncavitating conditions).

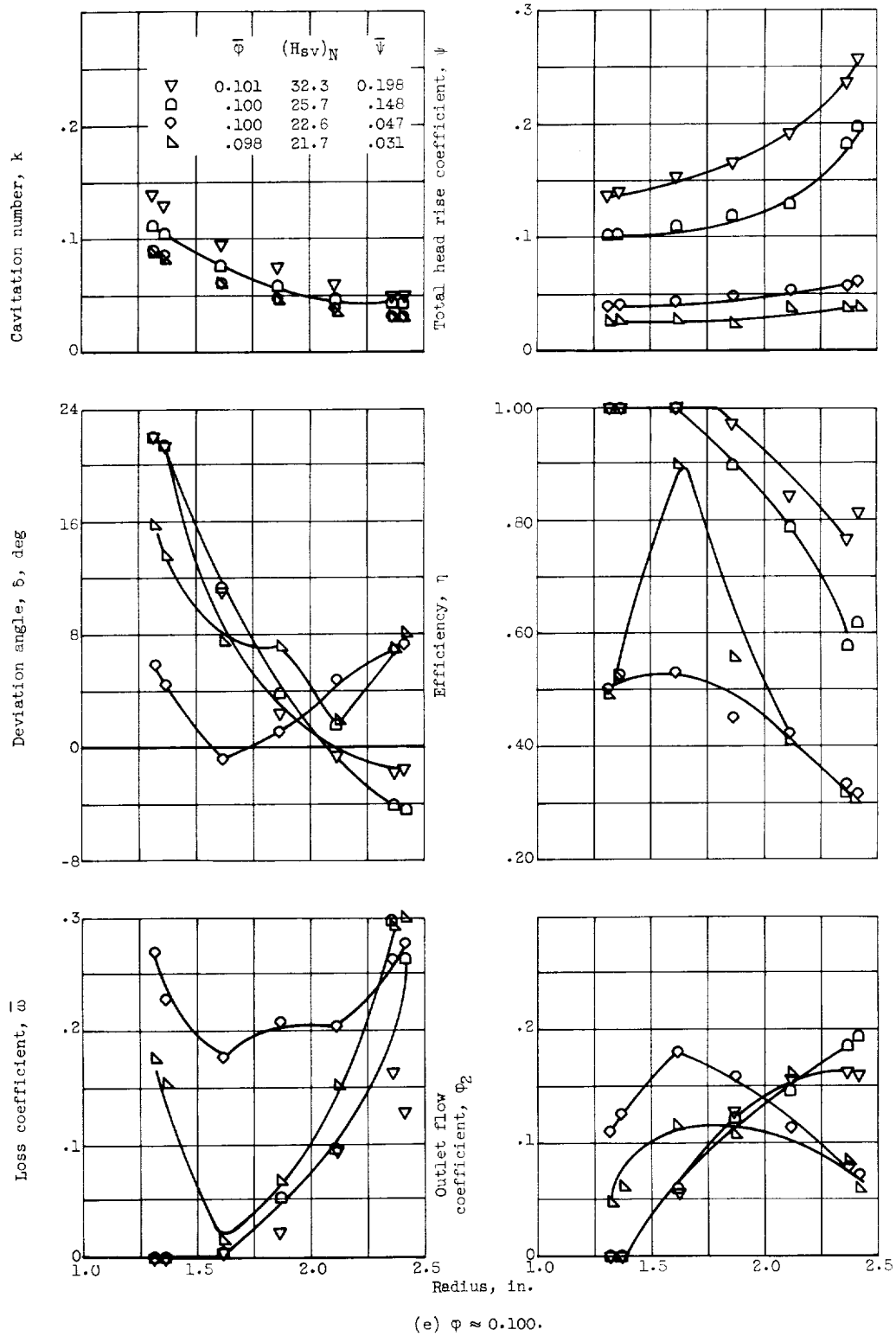


Figure 18. - Continued. Radial distribution of flow conditions and blade-element performance parameters (cavitating and noncavitating conditions).

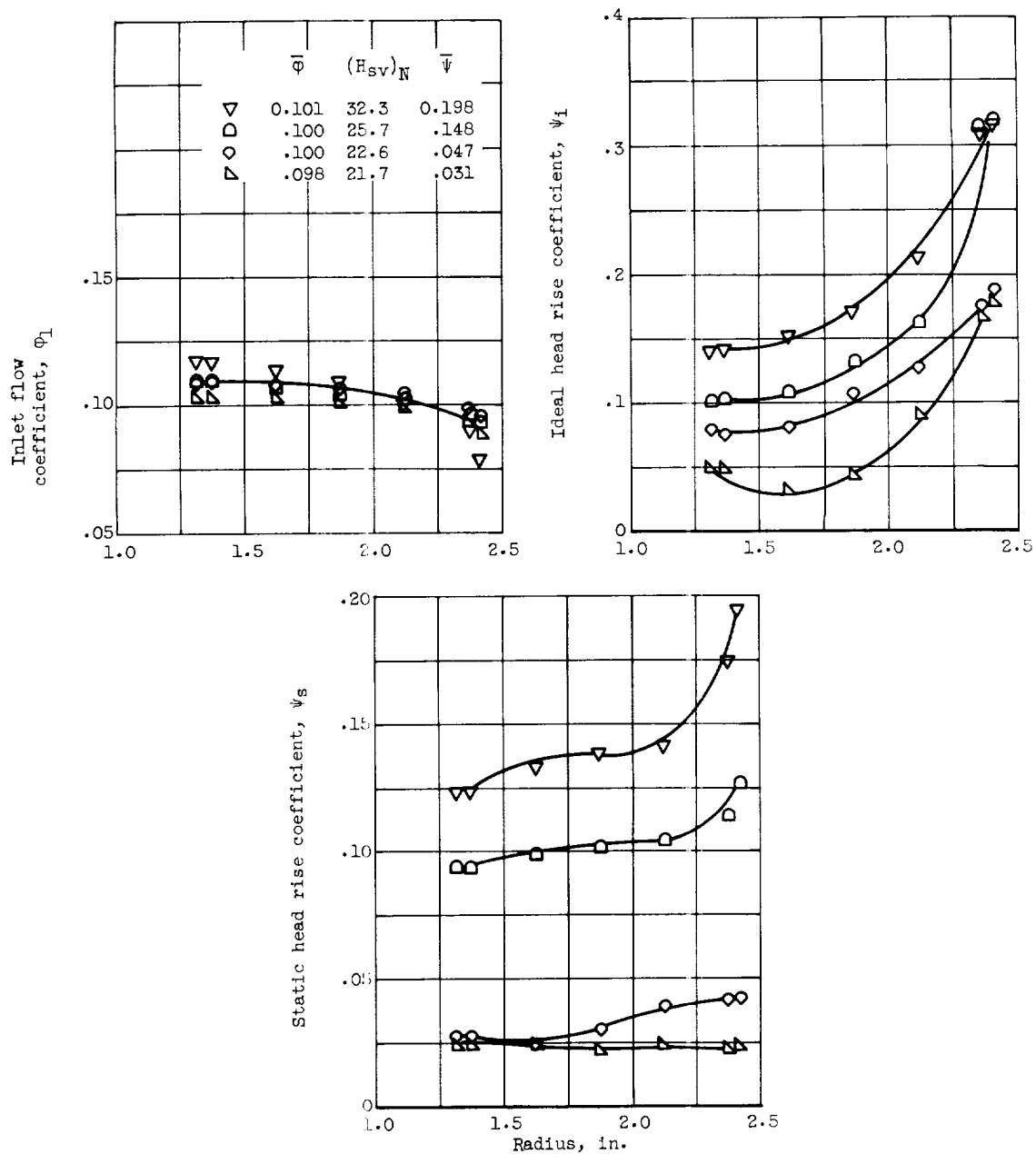
(e) Concluded.  $\phi \approx 0.100$ .

Figure 18. - Continued. Radial distribution of flow conditions and blade-element performance parameters (cavitating and noncavitating conditions).

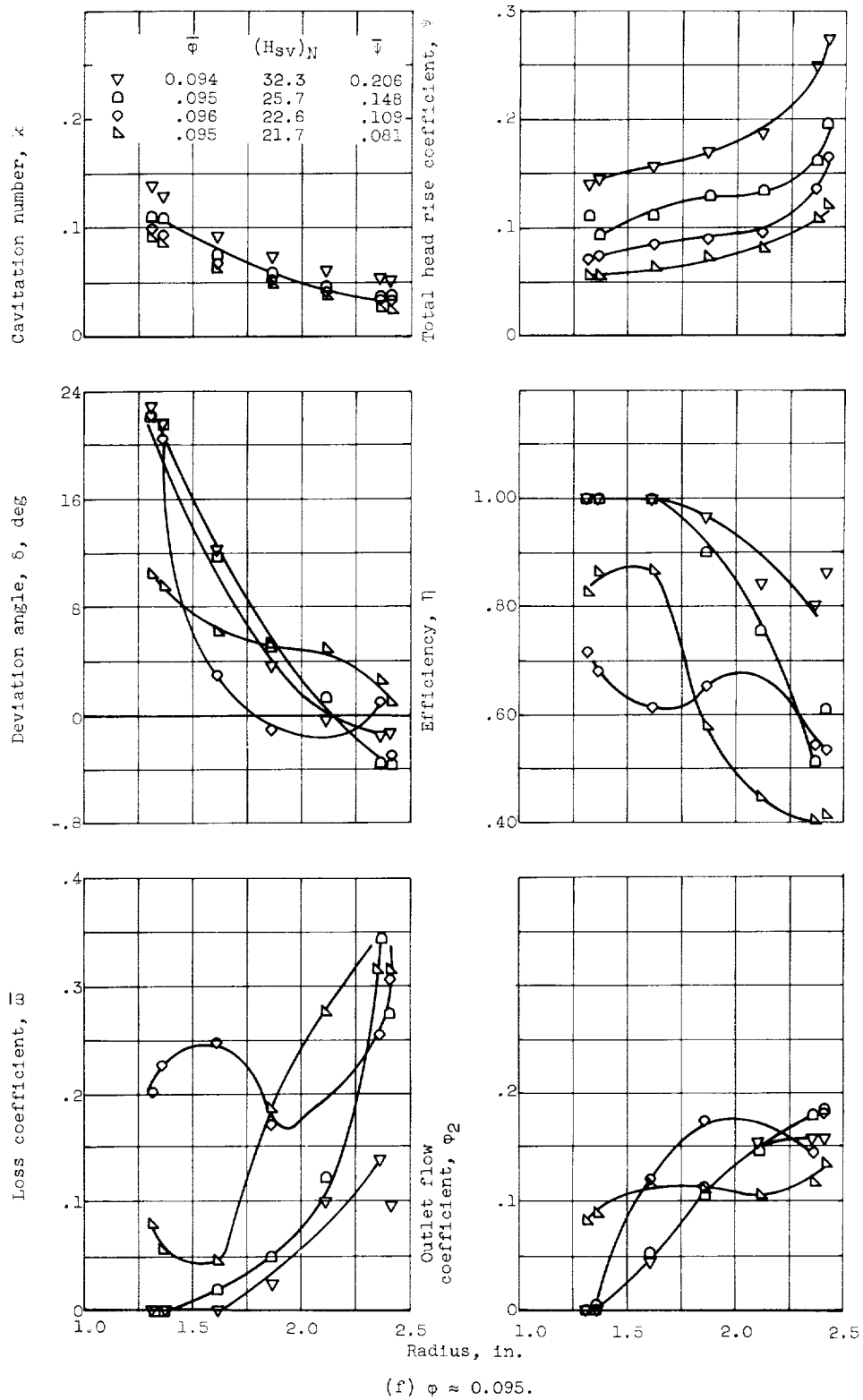


Figure 16. - Continued. Radial distribution of flow conditions and blade-element performance parameters (cavitating and noncavitating conditions).

E-1368

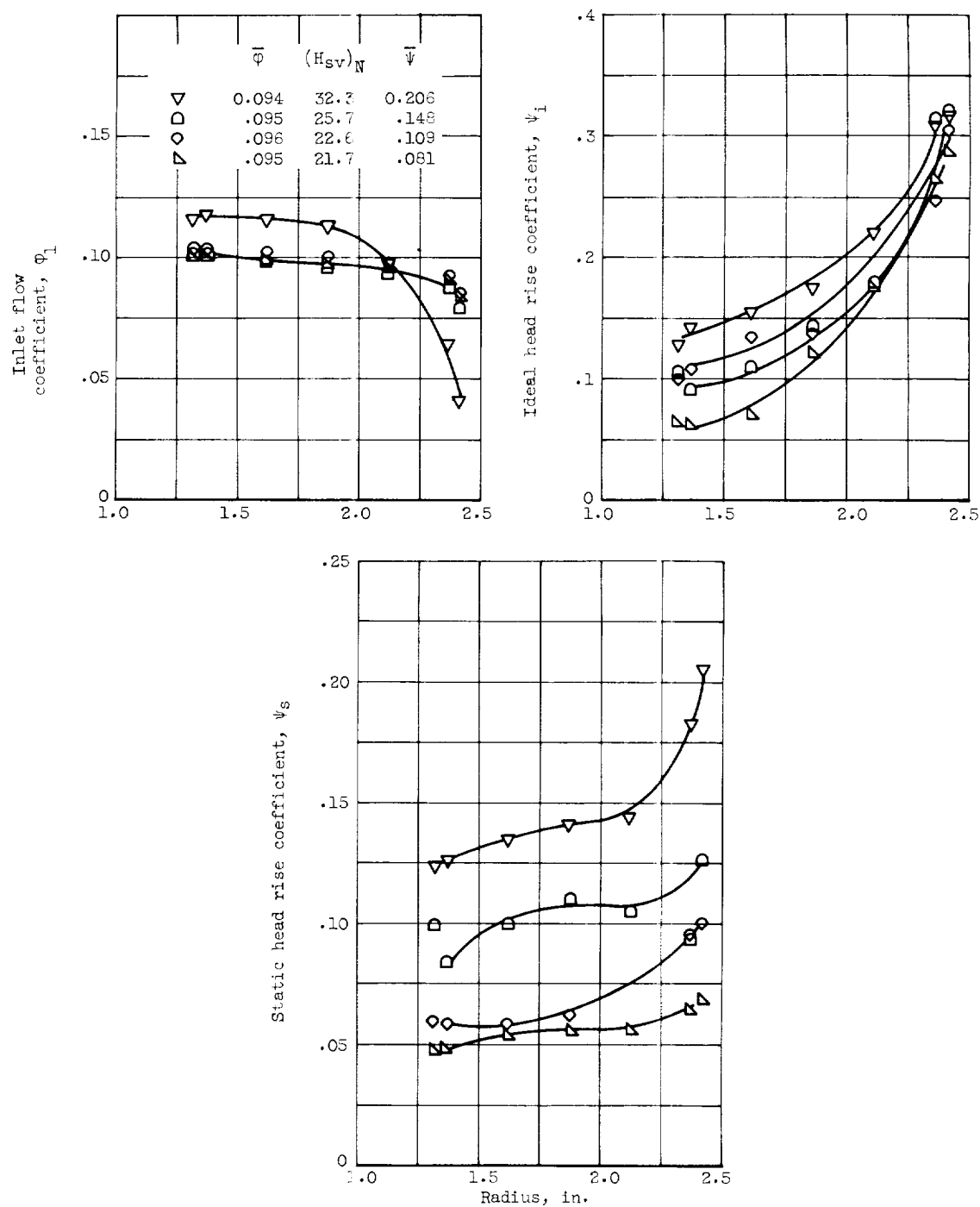
(f) Concluded.  $\phi \approx 0.095$ .

Figure 16. - Continued. Radial distribution of flow conditions and blade-element performance parameters (cavitating and noncavitating conditions).

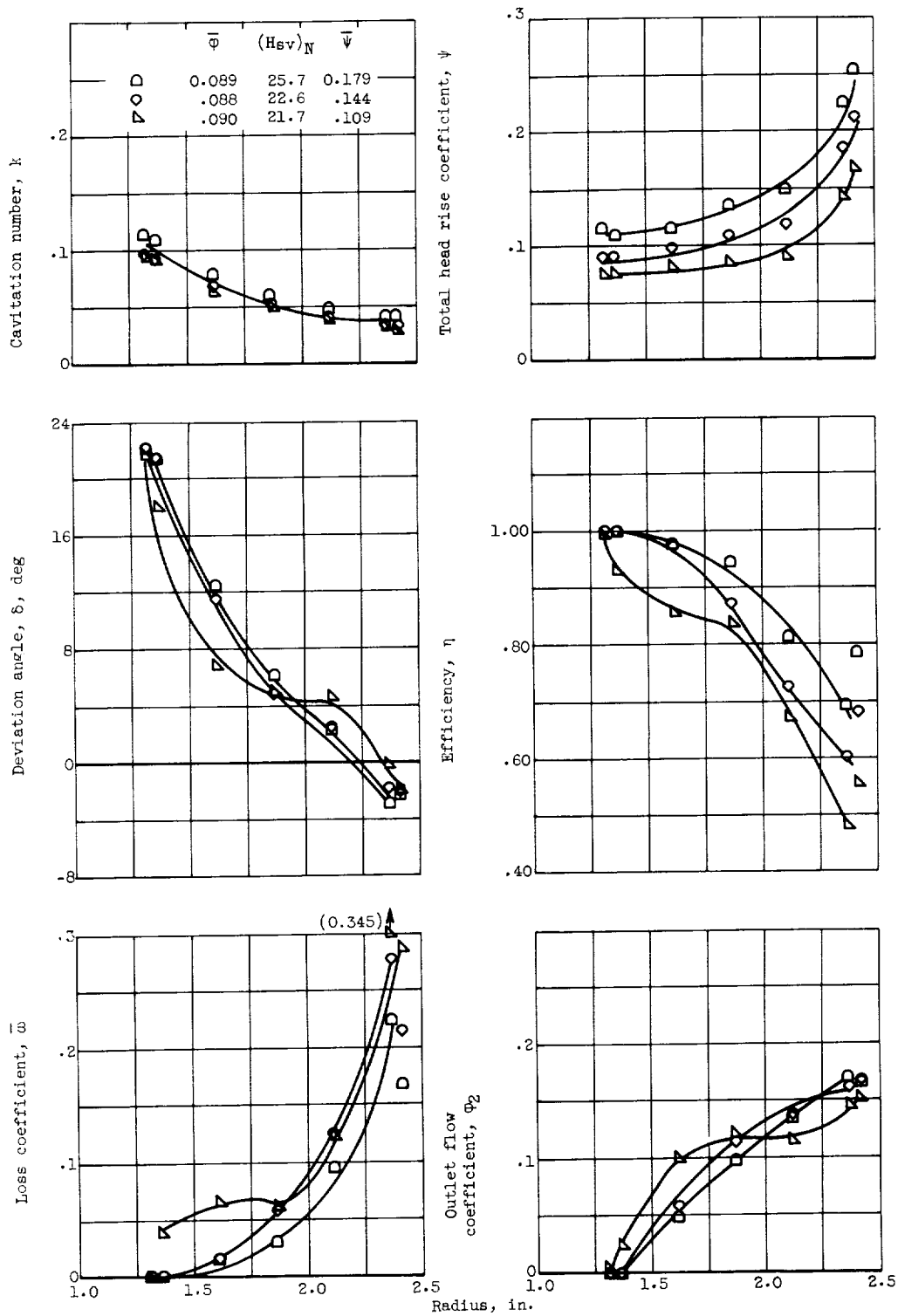
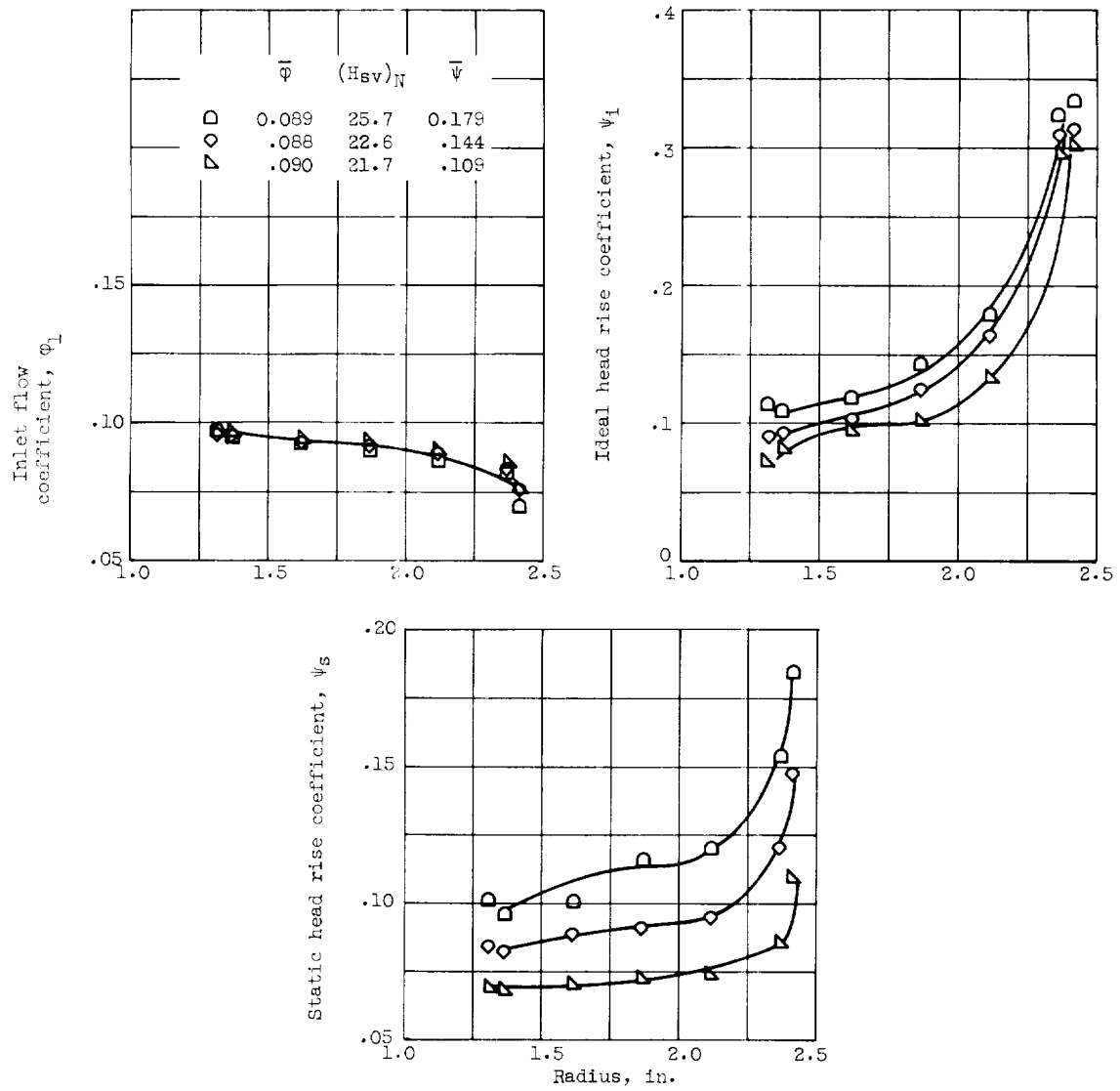


Figure 18. - Continued. Radial distribution of flow conditions and blade-element performance parameters (cavitating and noncavitating conditions).





(g) Concluded.  $\phi \approx 0.090$ .

Figure 18. - Concluded. Radial distribution of flow conditions and blade-element performance parameters (cavitating and noncavitating conditions).

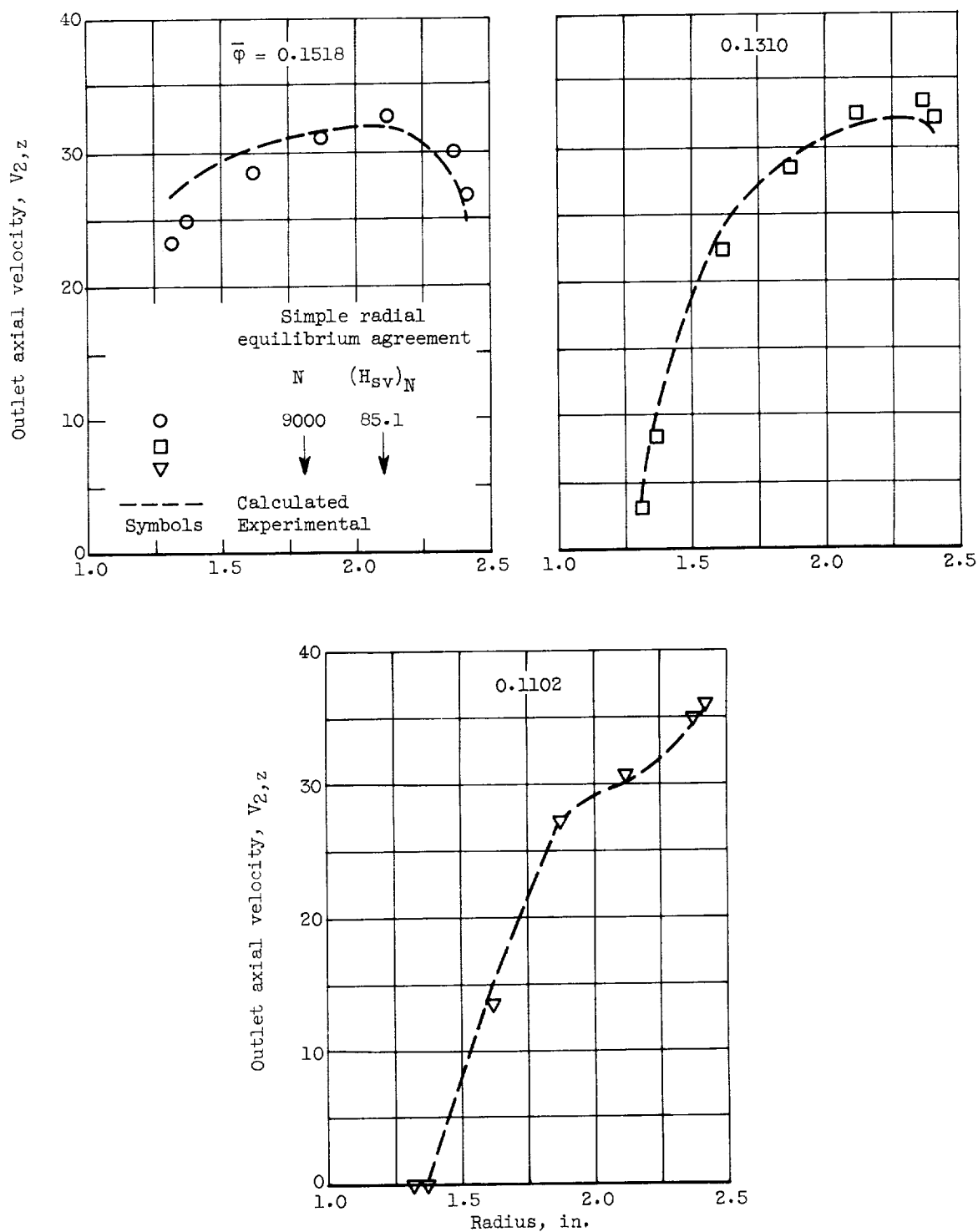


Figure 19. - Comparison of radial distribution of axial velocity as measured and as calculated using simple radial equilibrium equation.

E-1368

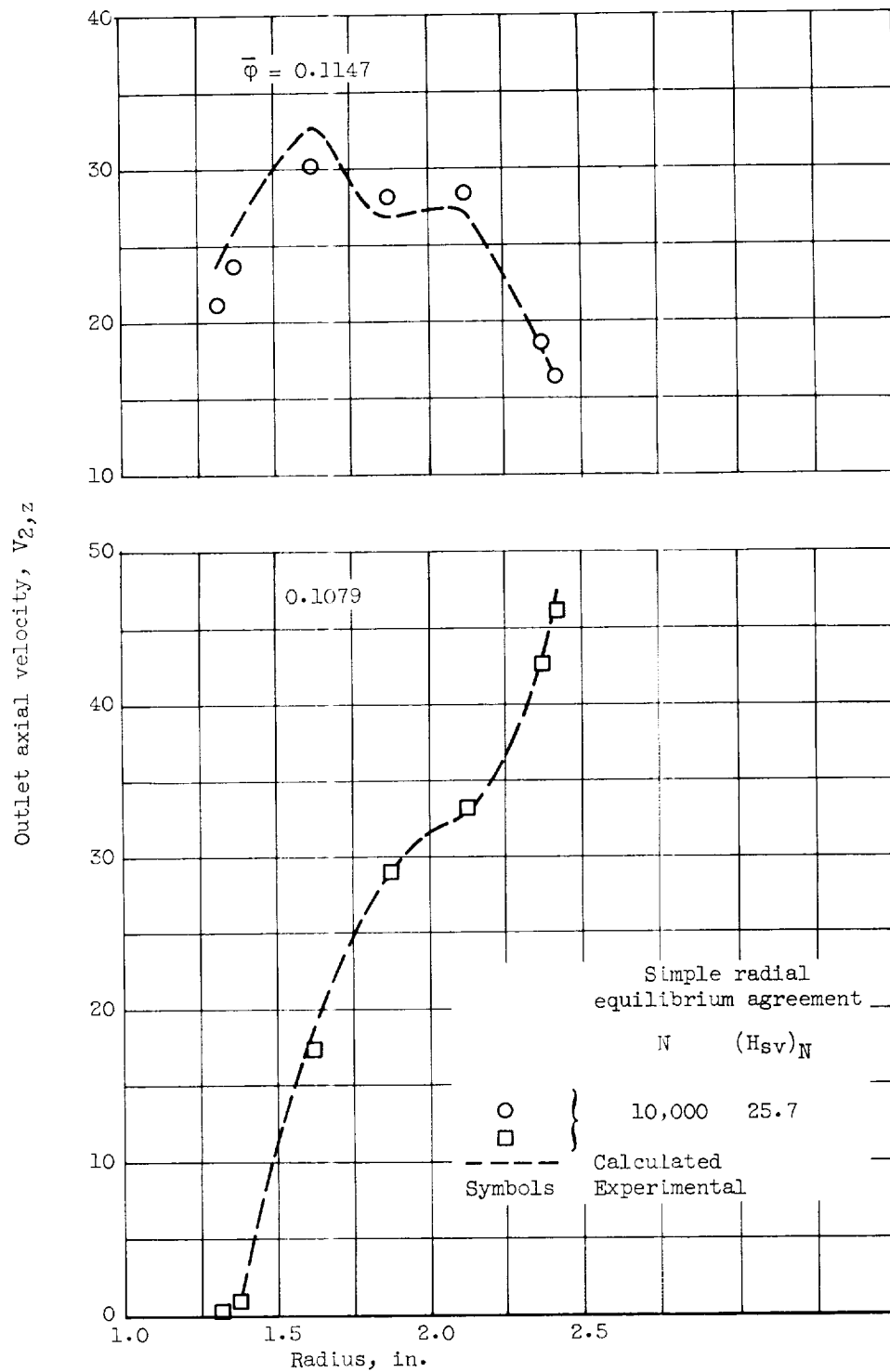


Figure 19. - Continued. Comparison of radial distribution of axial velocity as measured and as calculated using simple radial equilibrium equation.

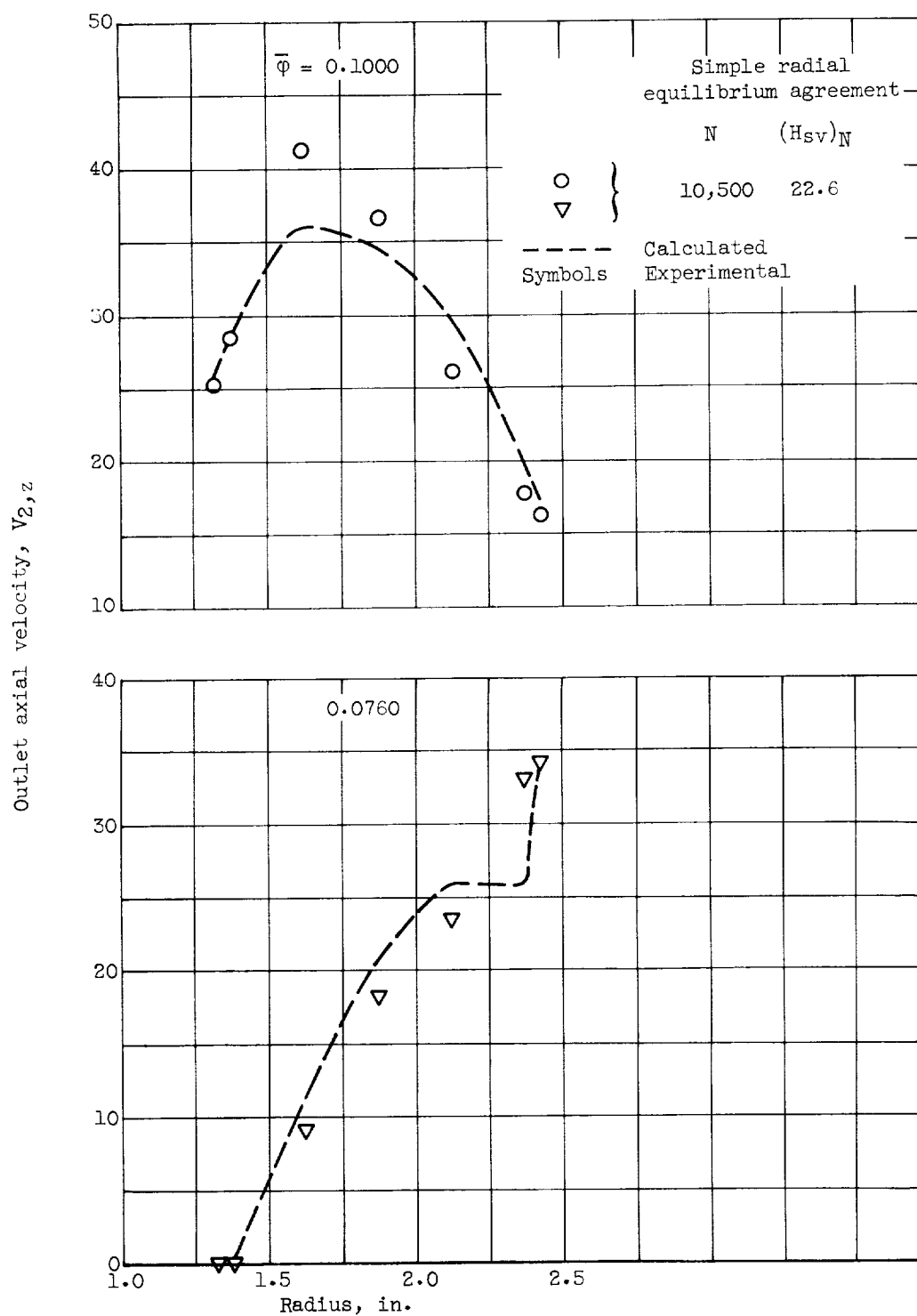
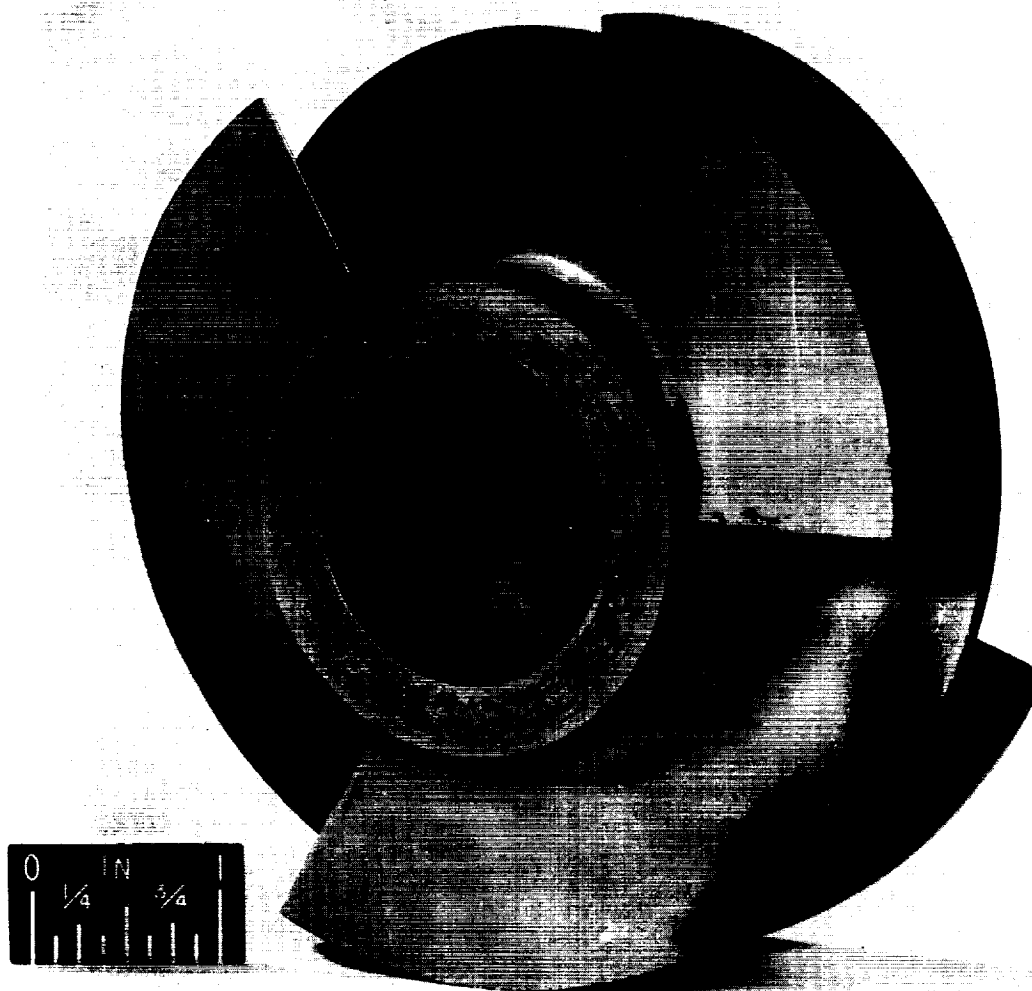


Figure 19. - Concluded. Comparison of radial distribution of axial velocity as measured and as calculated using simple radial equilibrium equation.



Figure 20. - Closeup of cavitation damage observed on 78° helical inducer.



C-55431

Figure 21. - 78° Helical inducer showing location of cavitation damage on blade suction surface.